Journal of Manufacturing Systems 82 (2025) 478–496

Contents lists available at ScienceDirect

Journal of Manufacturing Systems

journal homepage: www.elsevier.com/locate/jmansys

Technical paper

Quick dimensional inspection for continuous welding and assembly using machine learning-powered smart jig

Seobin Park [a,1], Taekyeong Kim [a,1], Kyeong Min Kim [c], Junyoung Seo [a], Jongwon Chung [d], Jeong Ho Choi [c], Wooseok Ji [a], Im Doo Jung [a,b,*]

[a] Department of Mechanical Engineering, Ulsan National Institute of Science and Technology (UNIST), Ulju-gun, Ulsan 44919, Republic of Korea
[b] Artificial Intelligence Graduate School, Ulsan National Institute of Science and Technology (UNIST), Ulju-gun, Ulsan 44919, Republic of Korea
[c] Manufacturing Solution Division, Factory Automation Engineering Department, Hyundai Motor Company, Buk-gu, Ulsan 44259, Republic of Korea
[d] Technological Collaboration Team, Hyundai NGV, Seoul National University, Gwanak-gu, Seoul 08826, Republic of Korea

ARTICLE INFO

Keywords:
Anomaly detection algorithm
Machine learning
Multivariate time-series data
Automated quality inspection
Sensor embedding
Total inspection

ABSTRACT

In the mass production of metal-based products such as automobiles, continuous welding and assembly processes are essential. The final product is created through multiple stages of welding, and the cumulative misalignment at each stage can lead to excessive residual stresses or dimensional defects in the product. To compensate for these issues, design modifications or significant post-processing costs have been required. Traditional dimensional inspection methods, whether manual or automated, are limited in their ability to keep pace with the speed required for mass production, as they focus on point-by-point measurements. While 3D vision-based methods offer a solution, they are often costly and primarily suited for macro-scale inspections. Here, we propose a machine learning-powered smart jig that enables precise, micro-level dimensional quality monitoring during production, without interrupting the continuous manufacturing process. This method, designed for direct integration into continuous assembly welding lines, reduces inspection time from 12 min to 2.79 s, enabling the detection of dimensional errors at the 500 μm level. Demonstrations conducted on the production line at a commercial automobile manufacturer confirm the feasibility of this approach for comprehensive subassembly inspections during mass production. This system is expected to be highly adaptable for various manufacturing domains utilizing assembly jigs, offering transformative potential in quality inspection processes.

1. Introduction

Dimensional quality control (QC) is a critical task for zero-defect manufacturing [1–6] and ensuring flawless mass production in the automotive industry [7]. A single vehicle body comprises dozens of subassemblies, each precisely assembled by welding numerous components [8]. If minor dimensional deviations [9] of these components accumulate during this process, it can lead to issues such as body distortion due to residual stress [10,11], water leakage, or collisions of moving parts [12,13]. These problems are often detected only after a significant portion of the subassembly has been completed, either during intermediate or final inspection stages [14], resulting in unnecessary production losses.

The automotive industry traditionally relies on manual and random

Abbreviations: QC, Quality control; QI, Quality inspection; AI, Artificial intelligence; LiDAR, Light detection and ranging; MTS, Multivariate time-series; CNN, Convolutional neural network; LSTM, Long short-term memory models; RNN, Recurrent neural networks; USAD, Unsupervised anomaly detection a multivariate time series; CAE-M, Deep convolutional autoencoding memory network; MAD-GAN, Multivariate anomaly detection with generative adversarial networks; NG, Defective case; OK, Normal case; TPU, Thermoplastic Polyurethane; ML, Machine learning; GUI, Graphical user interface; FDM, Fused deposition modeling; FEA, Finite element analysis; $Threshold_c$, Clamping threshold; QuickDimML, Quick dimensional inspection machine learning model; DM_i, Door member; POT, Peak over threshold; D, Decoder; E, Encoder; x_i, Data at i^{th} timestamp; x', Normalized data; x_{min}, Minimum value of timestamps; x_{max}, Maximum value of timestamps; ε, Small constant; s_j, Sensor j; O_1, Reconstructed output 1; O_2, Reconstructed output 2; $\dot{O}_2$, Reconstructed output 2 form the phase 2; S, Average score; $\widehat{X}$, Test data; t_0, The time point at which the part is clamped; t_c, The time point at which the average value of the data exceeds the clamping threshold.

* Corresponding author at: Department of Mechanical Engineering, Ulsan National Institute of Science and Technology (UNIST), Ulju-gun, Ulsan 44919, Republic of Korea.
E-mail address: idjung@unist.ac.kr (I.D. Jung).
[1] Equal contribution

https://doi.org/10.1016/j.jmsy.2025.07.001
Received 19 December 2024; Received in revised form 16 May 2025; Accepted 2 July 2025
Available online 10 July 2025

sampling-based quality inspections (QI) during production [15] (Fig. 1a). Skilled workers load randomly selected parts onto a checking fixture and manually measure critical dimensions using a dial gauge and perform visual inspection [16,17]. However, this method relies heavily on operator experience [18], which leads to prolonged inspection times per part. Detecting minor defects in unpainted panels also remains a challenge, even for experienced inspectors. It is practically impossible to inspect all intermediate products on every assembly production line. Manual inspection accuracy typically varies between 75 % and 90 %, depending on the inspector's experience and fatigue level [19], with the target defect detection rate generally set at 85 % or higher [20]. Consequently, undetected defects may persist in inspected parts, and uninspected products may still contain defects [3,21,22].

To address these limitations, advanced technologies such as artificial intelligence (AI) [23–25], touch probe measurement systems [26], vision-based quality monitoring technologies [27–29], non-contact coordinate measuring methods using laser scanning [26,30,31], and LiDAR [32] have emerged. These techniques reduce human error but often require costly equipment and are constrained by the size of measurable parts. Recent research has shifted towards leveraging time-series data collected from sensors embedded in equipment [33–35] to predict defects [36], equipment failures, and component lifespan [37–40], when anomalies in time-series data deviate from the normal patterns [41,42]. These methods allow for cost-effective equipment management and defect prevention [43] but remain limited in handling real-time QI for individual products. Moreover, capturing the specific state and severity of defects solely through single time-series data is challenging. In that sense, multivariate time series (MTS) data, obtained from multiple sensors, presents opportunities for more complex and accurate anomaly detection [44–50]. The MTS data can reveal intricate relationships between temporal sequences and various variables [51,52]. However, challenges such as the lack of anomaly labels, data volatility, and the need for rapid inference times complicate the implementation of MTS-based systems [53]. Algorithms such as CNN-based methods [52,54–56], unsupervised learning autoencoders [57], and LSTM-RNN-based GANs [58], have been proposed for real-time anomaly detection, but these models often require extensive computation and struggle with capturing long-term trends [53]. This highlights the need for further research to manage and analyze MTS data in industrial environments efficiently. Anomaly detection in MTS data must consider the sequential nature of multiple timestamps [59] and given the ambiguity in labeling defects (NG) and normal (OK) cases, it is essential to reflect the complex relationships between the temporality of data and variables [23]. To address this need, deep transformer networks have been demonstrated to be highly effective for quality inspection tasks involving MTS data due to their ability to capture long-range dependencies and complex relationships across multiple features [53,60]. The attention mechanism inherent in transformers allows them to focus on relevant time steps, regardless of their distance in the sequence, making them particularly suitable for detecting defects

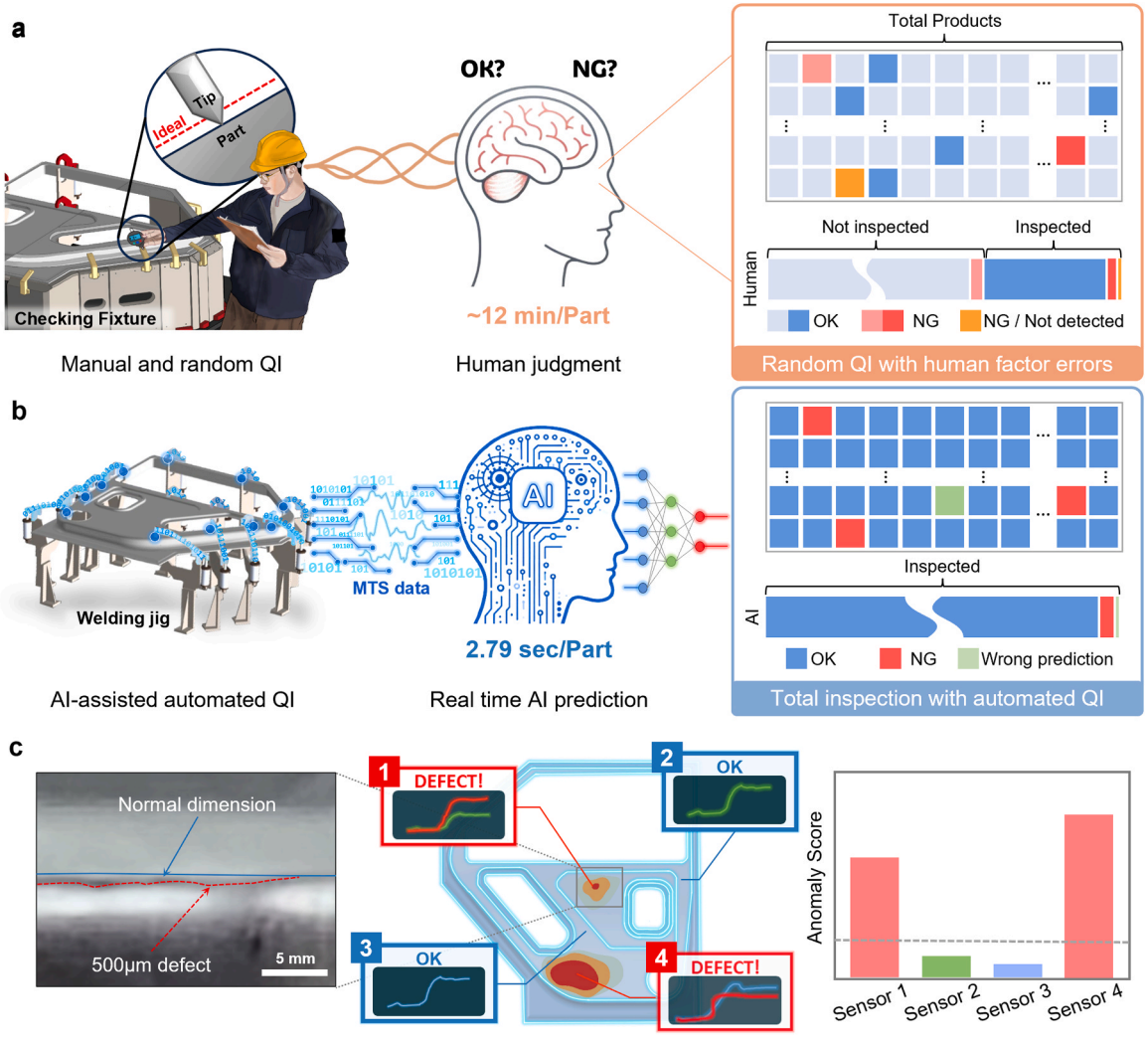

Fig. 1. A comparison of the traditional manual QI method and the AI-assisted automated QI system.

that span across different time points and dimensions.

In this article, we propose a real-time, automated, in-line QI system using a machine learning (ML) approach based on deep transformer networks for anomaly detection to process MTS data. As shown in Fig. 1**b, c,** the system uses lab-made sensors on the welding jig to detect dimensional errors as small as 500 μm at various clamping positions. Our system enables ultra-fast QI per part in just 2.79 s (Fig. 1**b**), compared to several minutes required by traditional QI methods (Fig. 1**a**). This is achieved by promptly identifying anomalies in MTS data in real-time and distinguishing them from normal data. Furthermore, given the industrial environment's predominance of normal products, the consistency of MTS data trends for normal cases enables the development of highly accurate AI models with minimal data training. Finally, the performance of this system was validated through its application on a production line for vehicle door parts at a commercial automobile company. As the proposed QI method enables anomaly detection from MTS data during manufacturing, it is broadly applicable to other complex assembly domains, such as aerospace and heavy equipment manufacturing.

The rest of this paper is organized as follows: Section 2 provides a detailed description of the hardware and software components of the proposed QI system. This includes the working principles of the sensor module developed to detect micro-scale dimensional defects, the process of collecting MTS data, the transformer-based ML model for real-time anomaly detection, parameter optimization methods, and a custom graphical user interface (GUI) environment designed for operators. Section 3 describes the experimental setup and the simulation of defects in both single and assembly parts. Section 4 presents extensive experimental results and discussions. Finally, the paper concludes in Section 5, where future research directions and the potential implications of the study's findings on smart manufacturing and autonomous QI systems are discussed.

2. Proposed real-time micro-level dimensional inspection method

Integrating a new QI system into an existing production system poses challenges, particularly in developing suitable sensors for defect measurement and managing the risks associated with modification of production systems. Automobile companies that operate based on accumulated expertise over decades often adopt a conservative stance toward technological changes that impact quality and safety [61]. Thus, bold investments and risk-taking are necessary to redesign and implement a QI system on-site. Therefore, applying a new QI system in industrial settings requires the following conditions: (1) high compatibility with existing equipment and systems, (2) easy sensor attachment and detachment for simplified maintenance, (3) cost-effectiveness to facilitate application across multiple production lines.

The smart welding jig for the real-time QI system consists of four major components: a welding jig (Figs. 2**a**), 3D-printed strain gauge-embedded sensor caps (Fig. 2**b**), data acquisition (DAQ) equipment (Fig. 2**c**), and a GUI environment (Fig. 2**d**).

2.1. Sensor cap

2.1.1. Fabrication

The lab-made sensor cap has the following characteristics. We have developed a novel sensor module for measuring dimensional deviations of automobile parts in welding jigs. The strain gauge-based sensor cap comprises a strain gauge sensor module (BF350–3AA, with a nominal resistance of 350 Ω and fatigue life of $> 10^7$ times) and a 3D printed sensor cap made of a Fused Deposition Modeling (FDM) printer (Ultimaker S3) with TPU 95 A filament (Ultimaker, with hardness of 48 Shore D and 96 Shore A, elongation at break >560 %). The sensor caps can be custom designed to fit various dimensioned clamps, leveraging the design flexibility provided by 3D printing. Utilizing the versatility of 3D printing, the strain gauge can be embedded inside the sensor cap during the printing process (Fig. 3). The fabrication of the sensor cap involves four steps: Step 1. Printing 2 mm-thick bottom layers incorporating a cavity for sensor placement; Step 2. Pausing the print once the final layer of the designated space for the strain gauge is completed then attaching the strain gauge using cyanoacrylate adhesive (Tokyo Sokki) at the designated location; Step 3–4. Resuming the print to encapsulate the upper surface of the strain gauge using melted filament, thereby completing the remaining printing process. The bottom layers of the sensor cap are designed with a 50 % infill to enhance deformation flexibility.

The sensor readings measured at different clamp positions may exhibit varying trends due to multiple factors, including pressure deviations in the air cylinders actuating the jigs, non-uniform clamping forces caused by manufacturing tolerances of the jigs, differences in the geometry of the clamp contact surfaces, and local geometric variations of the panel at each clamping location. To prevent the sensors from operating at their limits, each sensor was individually calibrated using a trimmer potentiometer such that, under the reference pressure of 9.9 kgf cm^{-2} applied by the air piston, the sensor output would reach 80 % of its maximum value within the full measurement range (0–1024) when clamping a normal panel.

First, Fig. 2**b** illustrates the sensor cap, fabricated by 3D printing and custom-made to precisely fit various dimensions of contact surfaces on jig clamps. Second, the sensor cap can be easily attached and detached

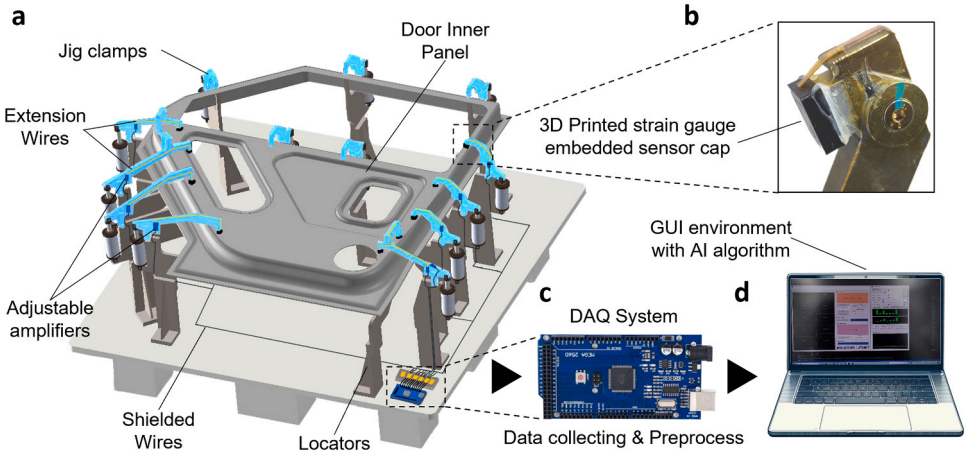

Fig. 2. Hardware system of the smart welding jig.

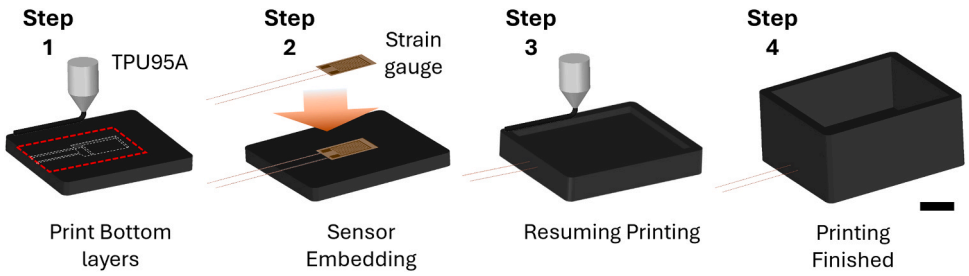

Fig. 3. The fabrication procedure of the strain gauge embedded sensor module via FDM printing (scale bar: 5 mm).

from the clamps, allowing for selective attachment to clamps at points that critically impact the quality of the automobile. Third, it offers universal applicability to diverse welding jigs and enables flexible sensor placement in terms of attachment positions and quantities. Therefore, the installation is highly convenient, as all components are low-cost and compatible with existing facility systems without any modifications.

2.1.2. *Working principle*

The working principle of defect detection of our QI system is illustrated in Fig. 4. Fig. 4**a** presents the example scenario of clamping a defective panel. Defects on the panel such as dings, dents, or bending induce subtle shape deformations across a wide area that are difficult to detect visually. Panels that deviate from the normal shape cause uneven deformations on the bottom surface of the sensor cap under compressive pressure (Fig. 4**b**).

2.1.3. *Finite element analysis*

The bespoke TPU 95 A based 3D printed sensor cap, attached to the clamp tip of a welding jig, enhances the measurement sensitivity of embedded strain gauge by leveraging material deformation induced by pressure during panel clamping. To conceptually validate the deformation mechanism of the sensor cap under clamping forces, its mechanical behavior was evaluated under the assumption that an arbitrary dimensional defect (~500 μm) existed in the vicinity of the sensor cap. The proposed methodology employs finite element analysis (FEA) simulations to examine whether dimensional defects that could impact welding quality near the sensor cap cause distinguishable differences in the deformation behavior of the sensor cap.

The FEA simulation was performed using the commercial software COMSOL. The material properties of TPU 95 A can deviate from those of the raw filament due to process-induced variations such as layer-by-layer deposition and internal infill settings in additive manufacturing [62–64] . In this study, the material properties of raw TPU 95 A (Young's

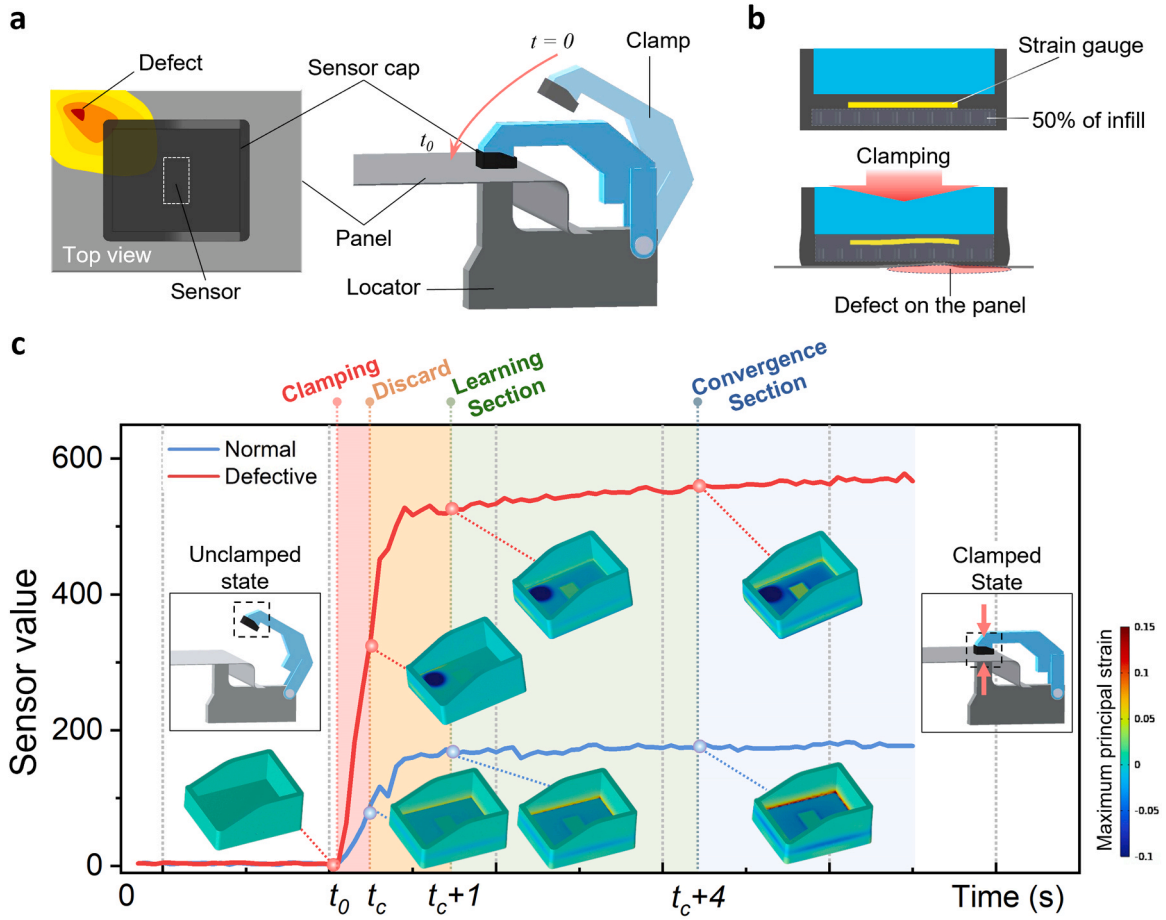

Fig. 4. Schematic illustration of the working principle for defect detection on the panel using the sensor cap and results of the FEA simulation.

modulus, E = 39 MPa; Poisson's ratio, $\nu = 0.4$; density, $\rho = 1.2$ g cm^{-3}) were assumed to investigate how panel defects influence the strain distribution of the sensor cap and to identify correlation patterns between defects and strain response. Simulation was conducted to evaluate the deformation and mechanical response of the sensor cap under a compressive load of 9.9 kgf cm^{-2}, representing clamping-induced compression. A vertically downward force was applied to the surface in contact with the clamp, while the surface in contact with the panel was assigned a fixed boundary condition. In addition, an arbitrarily shaped defect was also considered on the fixed surface, and a 500 μm upward displacement was imposed to model the corresponding deformation behavior.

Fig. 4**c** and Fig. 5 show FEA results of the sensor cap and the difference in trends of MTS data between normal and defective cases. The MTS data are measured at approximately 0 in the unclamped state with baseline noise. Then the strain value increases simultaneously with clamping (t_0), and it converges to a constant value a few seconds later. To quantitatively define the clamping onset, a clamping threshold ($Threshold_c$) was set at 150 which is the average strain value of all sensors, and that time point was defined as the clamping state (t_c). The measuring range is 0–1024 without units (Fig. 5), and the trends of sensor value vary depending on the bottom area of the sensor cap and the shape of the panel at each clamp position. In particular, Fig. 4**c** illustrates that the strain values and their time-dependent patterns differ significantly between normal and defective cases, as confirmed by FEA-based deformation simulations. These simulations reveal how the sensor cap undergoes sequential deformation depending on the surface geometry of the clamped panel. As the clamping force is applied, the sensor cap deforms in accordance with the local shape of the panel, and the resulting bending strains are recorded as multivariate time series data that reflect the panel's three-dimensional deviations.

The changes in this MTS data can be figured out through FEA results as differences in the degree of material deformation occur in the sensor cap when clamping both normal and defective panels. Defects on the panel lead to different trends in the measured strain values between normal and defective cases. The sensor made of ductile material is not only structurally stable enough to maintain its overall shape despite repeated impacts, but it is also sensitive enough to detect differences by causing local deformations due to minor defects. The results of the FEA simulation suggest that the presence and severity of structural defects can be readily assessed using the sensor cap. Furthermore, this approach can be further developed into a more efficient and accurate defect detection method across the entire panel by incorporating numerical techniques based on surrogate models [65] and adaptive sampling [66, 67], which are well-suited for exploring high-dimensional design spaces. Our method offers a highly efficient approach, as it relies solely on the characteristics of patterns within the MTS data, eliminating the need for complex and precise analysis of the forces applied to multiple clamps. This makes it particularly advantageous for universal application across various types of welding jigs.

2.1.4. Fabrication repeatability and durability test of the sensor cap

To comprehensively evaluate the reliability of the sensor cap, both fabrication repeatability and long-term durability tests were conducted (Fig. 6). As illustrated in Fig. 6**a**, five sensor caps fabricated under identical 3D printing conditions were mounted at the Sensor 1 position of the test jig. All five caps exhibited consistent sensor responses within an acceptable error range under clamping across time points. This confirms the excellent repeatability of the sensor cap fabrication process. In addition, a durability test was conducted to verify the long-term stability of the sensor performance (Fig. 6**b**). The durability test was conducted by attaching three sensors to the test jig. The sensors maintained consistent performance and measured constant values, without any degradation, over 1000 clamping cycles. The clamping time was set to 4 s, which is longer than the time required for QI, and the unclamping time was also set to the same 4 s.

2.2. DAQ system

Four sensors were installed in the test jig, and eight sensors were attached to the production jig in the real factory. The DAQ system was configured to acquire ten strain data points per second from the installed sensors. In addition, a first-order low-pass filter with a cutoff frequency of 4 Hz was applied, enabling the extraction of signal features by reducing sensor noise and eliminating the influences of interference data.

2.3. Quick dimensional inspection ML algorithm

In this work, we developed an ML model, QuickDimML (Quick Dimensional inspection ML model), capable of detecting outliers in MTS data with high accuracy and speed while clamping a panel for body manufacturing at various positions to detect subtle dimensional deviations. This QuickDimML model is based on a deep transformer network [53], designed to process real-time MTS data (Algorithm 1), and specializes in outlier detection.

The construction of the model and the entire process are based on Python 3.7 and Torch 1.13, along with other libraries. The training and experiments for all models were performed on a system equipped with an Intel i5–11400 CPU, 16 GB RAM, Nvidia GTX 1650 GPU, and Windows 10 operating system, which are commonly conducted in factory-built systems.

Algorithm 1. Real-time anomaly detection algorithm

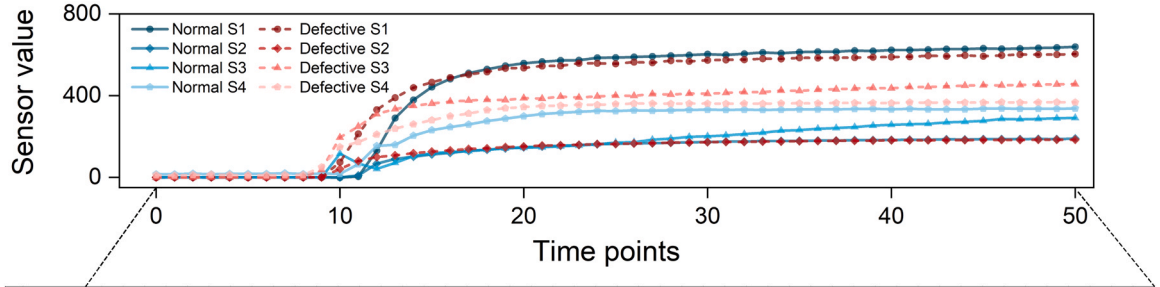

	Sensor #	1	2	3	4	5	6	7	8	9	10	11	12	13	14	15	16	17	18	19	20	21	22	23	24	25	26	27	28	29	30	31	32	33	34	35	36	37	38	39	40	41	42	43	44	45	46	47	48	49	50
Normal	S1	4	4	4	5	4	5	4	4	5	4	5	4	131	290	379	442	482	510	529	546	558	566	572	573	585	586	589	592	595	598	603	599	605	611	607	613	615	615	620	618	623	623	625	628	628	631	629	630	633	635
	S2	2	2	3	3	2	3	2	3	2	2	9	67	90	101	112	120	130	135	142	147	151	155	158	162	164	166	167	169	171	173	175	175	178	178	179	180	180	182	182	183	184	184	186	185	187	187	187	188	187
	S3	3	4	2	4	4	3	4	3	3	3	116	68	41	71	104	118	124	129	135	142	145	147	152	156	162	170	172	184	190	198	201	205	212	218	228	231	238	241	246	253	257	260	262	269	272	276	286	284	286	289
	S4	15	15	18	15	17	17	17	20	16	18	17	64	154	159	204	231	246	259	275	287	299	310	316	321	325	324	328	326	328	330	331	330	331	330	331	333	333	333	334	335	333	335	333	333	333	336	337	335	335	335
Defective	S1	4	5	5	5	4	5	4	4	5	5	74	213	331	390	439	465	488	503	516	534	535	545	546	558	558	556	564	561	571	568	573	575	576	581	580	585	584	585	586	588	589	590	595	593	597	593	597	601	601	601
	S2	3	3	2	3	3	2	2	3	2	3	41	80	99	108	118	126	132	139	142	148	151	156	157	159	163	163	166	167	170	170	172	173	173	175	175	177	178	179	179	180	181	181	181	182	182	183	183	183	184	184
	S3	4	4	3	3	3	4	3	3	4	37	195	249	310	334	350	361	371	376	380	378	388	385	395	391	396	400	399	408	405	410	409	414	417	417	425	423	429	431	435	438	436	442	442	446	449	451	450	452	454	455
	S4	11	9	12	14	12	10	10	12	12	50	148	173	210	239	260	280	299	312	329	338	344	349	351	355	355	358	361	361	360	361	361	360	361	360	362	362	362	364	364	364	363	367	365	367	366	366	368	366	367	368

Fig. 5. Trend comparison of MTS data points between normal and defective samples under the test jig.

Input: Real-time multiple strain data from the welding jig
Output: Predicted label with anomaly score
Require:
Trained Encoder E, Decoders D_1 and D_2
Clamping threshold T_{clamp} and Defect threshold T_{defect}
Number of sensors N
Detection length L
Detection status $S_{detection}$
Predicted label Y
Sensor data S[1,...,N] and Sensor series data A[1,...,L]
Minimum and maximum values of sensor series data A_{min} and A_{max}

$N \leftarrow n$
$T_{clamp} \leftarrow 150$
$S_{detection} \leftarrow True$
$cnt \leftarrow 1$
while $S_{detection}$ = True **do**
  for $i = 1$ to N **do**
    S[i] $\leftarrow$ Sensor data S_i ▷ Real-time data collection
  end for
  if $cnt \leq L$ and $mean(S) > T_{clamp}$ **then**
    $A[cnt] \leftarrow S$
    $cnt \leftarrow cnt + 1$
  end if
  if $cnt = L$ **then**
    $A' = \frac{A - A_{min}}{A_{max} - A_{min} + \epsilon}$ ▷ Min-max normalization
    $O_1 \leftarrow D_1(E(A', \vec{0}))$
    $\hat{O}_2 \leftarrow D_2(E(A', \|O_1 - A'\|_2))$
    $l = \frac{1}{2}\|O_1 - A'\|_2 + \frac{1}{2}\left\|\hat{O}_2 - A'\right\|_2$ ▷ Compute loss
    $y = \frac{1}{n}\sum_{j=1}^{n} l_j$ ▷ Calculate anomaly score
    $Y = \mathbb{1}(y \geq T_{defect})$
    Plot detection result y, Y
    $cnt \leftarrow 1$
    Initialize sensor series data A
  end if
end while

2.3.1. Data collection

Data collection was performed under controlled laboratory conditions as well as in an operational factory environment. Fig. 7 shows representative MTS data obtained from eight sensors integrated in the actual production jig in factory described in Section 3.2, illustrating distinct trend patterns corresponding to three clamping states unclamped, clamped with a normal panel, and clamped with a defective panel. MTS data can vary significantly depending on the type, location, and severity of defects. For example, excessive pressure applied to the sensor cap due to a defect may result in higher sensor values than normal. In comparison, incomplete clamping may show lower sensor values or time-series trends similar to the default state. Moreover, in cases where no defect is detected at the clamping position, the trend may exhibit a pattern similar to that of a normal panel. These trends can be observed immediately after clamping, highlighting the importance of data collection during this phase for effective training of the QuickDimML model.

We conducted data collection and performance evaluation of defect detection using lab-scale test welding jig with ten panels provided by a commercial automobile manufacturing company. Test samples consist of five normal samples and five reference defective samples with various defects located in different positions. Detailed explanations of the setup and samples are provided in Section 3.1. First, to assess the accuracy and consistency of the sensor measurements and to create the training and test datasets, we alternately clamped each sample and collected a total of 120 normal datasets and 20 abnormal datasets. As shown in Fig. 8, five normal parts were measured 24 times each, resulting in a total of 120 normal data sets, which fall within the 2σ standard deviation range, indicating that AI training does not require a large amount of data due to the high proportion of normal products in industrial conditions. In contrast, MTS data for defective samples are generally distributed well outside the normal range, showing distinct trends. However, when the defective region is not near a specific sensor, the corresponding time-series data may remain within the normal range, despite the presence of a defect in the part.

2.3.2. Data preprocessing and building datasets

The collected data were preprocessed through cropping and reorganizing to generate training and testing data. (Fig. 9**)**. To determine the optimal data segment length that enables accurate QI at the earliest possible time after clamping, we compared five different time ranges, as shown in Fig. 10. The initial 1-second interval immediately following the clamping state recognition point (t_c) was excluded due to potential disturbances caused by transient vibrations and noise during the clamping process. Therefore, F1 scores were evaluated for five data segments ranging from 2 to 6 s after t_c+ *1*. Among them, the segment corresponding to the first 3 s (50 data points) exhibited the highest F1 score of 0.9862. Based on this result, the collected raw data were cropped into specific regions labeled A to D and A* to D*, which were subsequently used to construct the training dataset (Fig. 9**a**) and test dataset (Fig. 9**b**), respectively. The cropped data were then merged into a single file for learning, and Min-max normalization was applied to each sensor between 0 and 1, as shown in Eq.1.

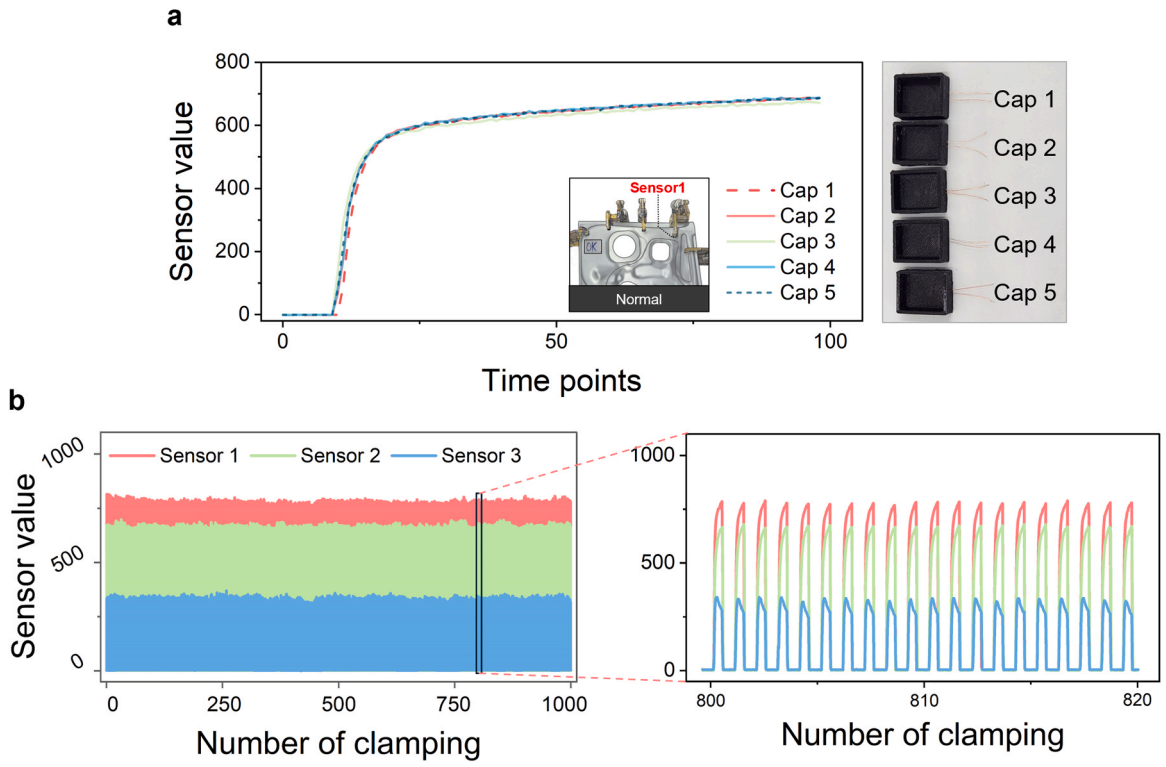

Fig. 6. Fabrication repeatability and durability test results of sensor caps.

$$x' = \frac{x - x_{\min}}{x_{\max} - x_{\min} + \varepsilon} \tag{1}$$

where a small constant (ε) is employed to prevent dividing by zero errors.

We randomly divided the training and test datasets into a 100:40 ratio. The training dataset was constructed by randomly selecting 50 data points from each of the 100 normal datasets, resulting in a total of 5000 data points (Fig. 9**a**). The test dataset included 50 data points from the remaining 20 normal and 20 defective datasets, concatenated in random order to yield 2000 data points (Fig. 9**b**).

2.3.3. Model architecture

In this study, a transformer model is employed to detect anomalies in the car door assembly process from the MTS data collected from sensors. The transformer was originally developed for natural language processing, where it processes an input sequence with multiple attention-based transformations [60]. The encoder processes the input sequence using a stack of self-attention and feed-forward layers. Each position in the sequence attends to all other positions via multi-head self-attention, allowing the model to capture both local and long-range dependencies without recurrence. The decoder generates output sequences by attending to both the encoder output (via encoder-decoder attention) and its own previous outputs. As shown in Fig. 11**a**, for the case of MTS data, the encoder processes the entire sequence up to the current timestamp C, assigning focus scores which is the reconstruction loss for the first decoder. Using this information, the window encoder generates an encoded representation of the input window W, which is then reconstructed by two decoders. The first decoder attempts to perfectly reconstruct the input window W (*i.e.*, $O_1 = W$), thereby generating a degenerate (zero vector) focus score to fool the second decoder. However, the second decoder attempts to distinguish between the input and the reconstruction from phase 1 by maximizing the difference $\|\widehat{O}_2 - W\|_2$ using the focus scores.

Therefore, by incorporating this algorithmic flow into our system, the prepared datasets were used to perform training and testing through a series of processes using QuickDimML (Fig. 11**a**, Algorithm 1). The QuickDimML model consists of an encoder, window encoder, and two decoders for reconstruction and prediction. The training process is composed of reconstruction of input window and optimization of attention weights. The MTS data are divided into a complete sequence corresponding to a sliding window and the current timestamp, which are each input into two separate encoders for adversarial training and reconstruction. The outputs from Decoder 1 and Decoder 2 (D_1, D_2) in Phase 1 are denoted as O_1 and O_2, respectively, and the result from D_2 in Phase 2 is represented as $\widehat{O}_2$. In phase 1, D_1 is trained to generate a focus score ($\|O_1 - W\|$) to deceive D_2, while D_2 is trained to produce an output O_2 similar to the input. In phase 2, D_2 learns to differentiate between W and the reconstruction generated by D_1 in phase 1. Consequently, the training objective of the QuickDimML was defined as follows:

$$\min_{D_1} \max_{D_2} \|\widehat{O}_2 - W\|_2 \tag{2}$$

In addition, the average score (S) for test data ($\widehat{W}$), which was not used for training, is as follows.

$$S = \frac{1}{2}\|O_1 - \widehat{W}\|_2 + \frac{1}{2}\|\widehat{O}_2 - \widehat{W}\|_2 \tag{3}$$

The result of the anomaly prediction by QuickDimML is visualized in Fig. 11**b**. The QuickDimML model accurately sorts out the locations of abnormal segments within the input test raw dataset, providing an anomaly score for each sensor. The high-abnormality segments are highlighted in red, and they precisely match the unlabeled true anomaly of the test dataset highlighted in orange in Fig. 9**b**. The results of our QuickDimML model indicate its capability to accurately detect anomalies within a dataset where normal and defective MTS data are randomly intermixed without distinct separation.

The F1 score is defined as the harmonic mean of precision and recall (Eqs. 4–6), and it is a widely used metric to evaluate the performance of classification models, especially in various industrial applications where the dataset is imbalanced [68–70].

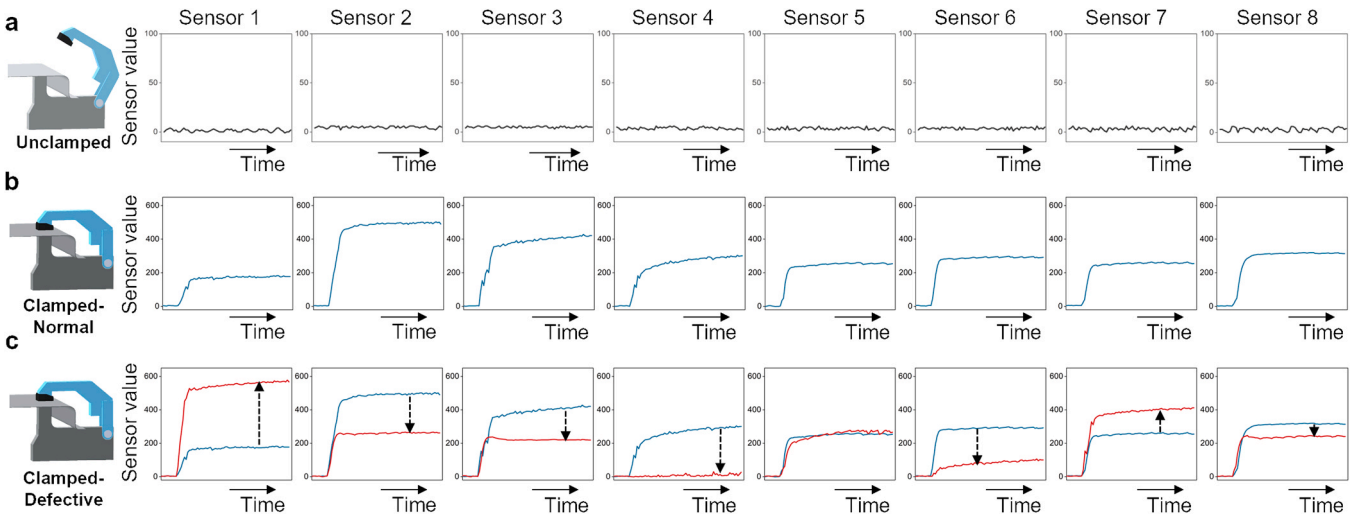

Fig. 7. Trend of MTS data according to the sensor position and parts qualities.

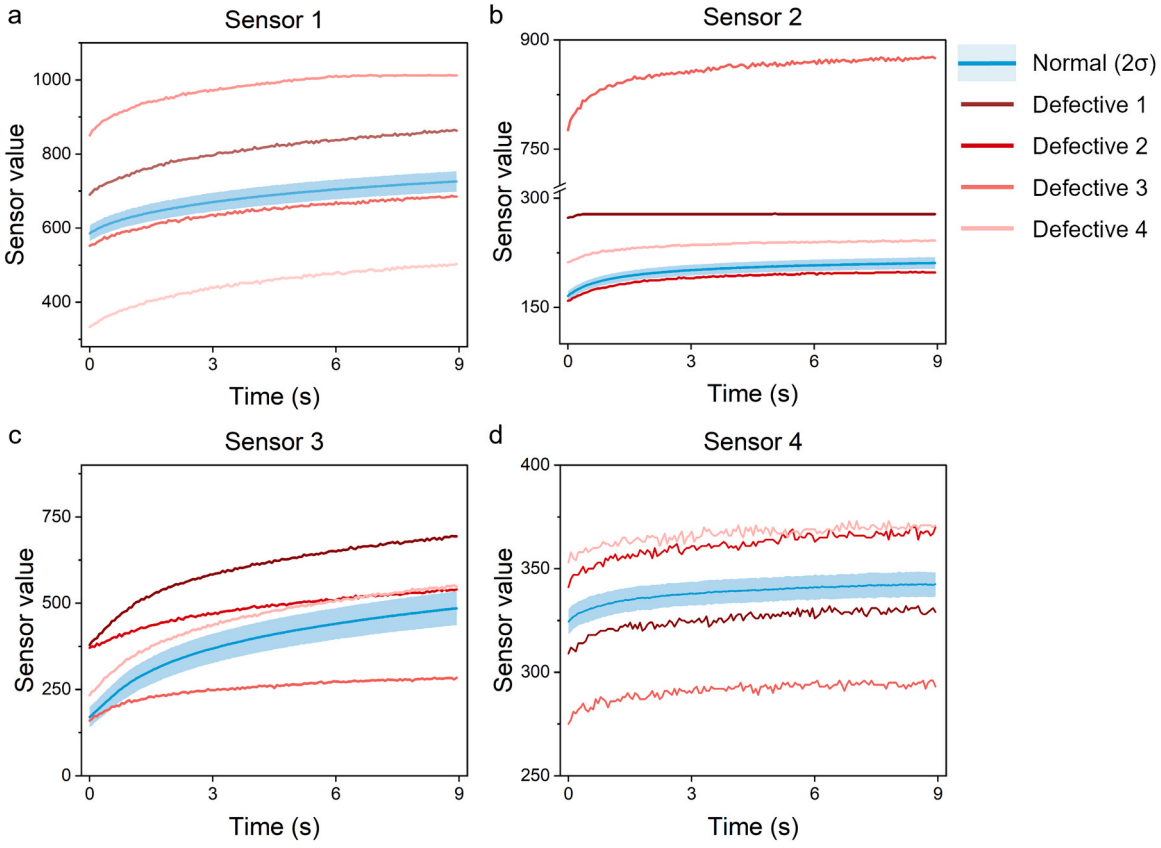

Fig. 8. Comparison of the MTS data between normal and defective parts across sensors.

$$Precision = \frac{TP}{TP + FP} \tag{4}$$

$$Recall = \frac{TP}{TP + FN} \tag{5}$$

$$F1\ Score = 2 \times \frac{Precision \times Recall}{Precision + Recall} \tag{6}$$

For the QI system, the F1 score was selected over other metrics, such as precision, recall, or area under the receiver operating characteristic curve, because it provides a single, interpretable metric that reflects both the system's ability to correctly identify defective components (recall) and its ability to avoid misclassifying normal components as defective (precision).

2.3.4. *Parameter optimization*

The optimal parameter for the QuickDimML model and its performance are evaluated in Fig. 12, Fig. S1, and Table 1. The relationship between the training loss (Fig. 12**a**) and the F1 score (Fig. 12**b**) over epochs shows that, while training loss converges to zero as the number of epochs increases, the highest F1 score (0.9862) was achieved at epoch 5. This means that the epoch 5 for the best F1 score should be set as the

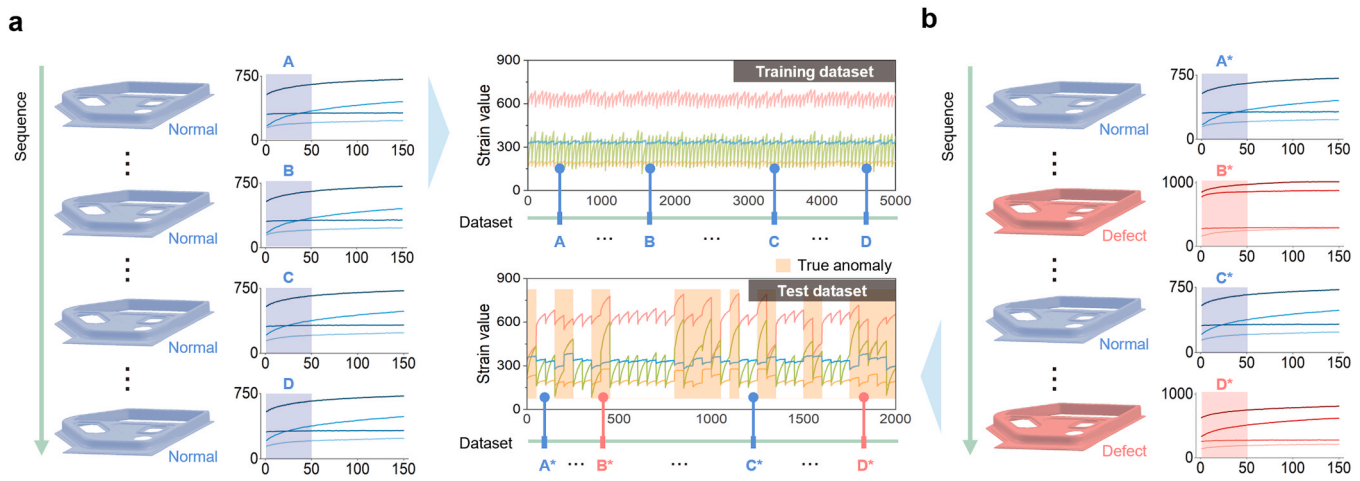

Fig. 9. Generating training and test datasets. (a) Training and (b) test datasets. Unlabeled true defective data in the test dataset highlighted in Orange.

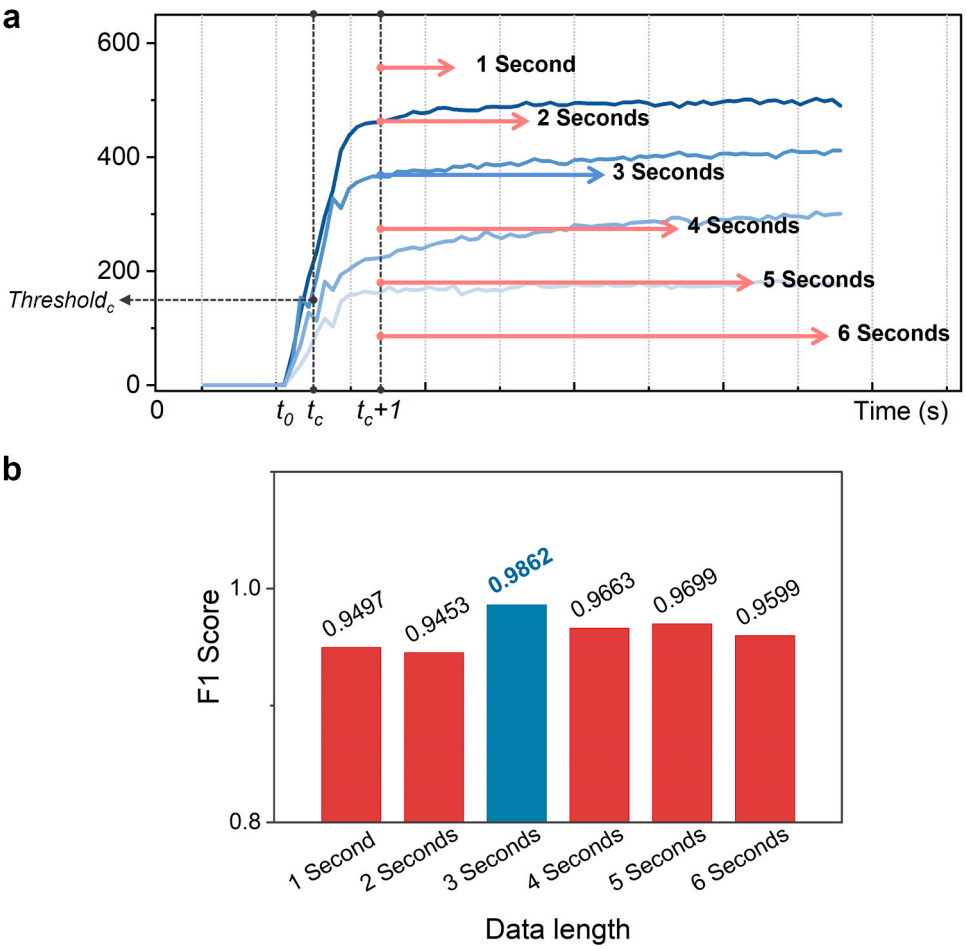

Fig. 10. Comparison of F1 scores based on the length of data points for model training. The physically clamped time point (t_0), the clamping detection point (t_c), the clamping state (t_c) clamping threshold (*Threshold*$_c$, 150).

optimal parameter for the QuickDimML model as follows the protocol in the previous studies [71,72]. The model was trained for five epochs and we utilized AdamW [73] as the optimizer with an initial learning rate of 10^{-3} and a weight decay of 10^{-5}. The F1 score, comprising recall and precision, was employed to evaluate the model performance. In addition, the performance of the QuickDimML model showed the best performance compared with that of USAD [57], MAD-GAN [58], and CAE-M [74] models, developed for anomaly detection (Fig. S1 and Table 1).

Peak over threshold (POT) [75] is used to classify the status of the part, determining it as anomalous if the anomaly score of the given time series exceeds the threshold. In addition, this method employs Extreme Value Theory to model the data distribution with a Generalized Pareto Distribution, enabling the dynamic determination of threshold values by

identifying the appropriate value at risk (Fig. 12**c, d**). From these algorithms, POT method automatically determines threshold levels without requiring manual specification or making assumptions regarding specific data distribution. Accordingly, the POT method has been utilized in numerous studies due to its advantages, and it is regarded as highly effective for its ability to select thresholds [75,76]. The proposed method was evaluated using two types of jigs (test jig and welding jig), for which two separate thresholds were computed by the POT method during model training, each rounded to the third decimal place. Here, to account for cases where the anomaly score for normal cases may lead to misjudgment due to slight variations, a margin was applied when setting the threshold.

2.3.5. Real-time defect detection performance

In an automated production line, dozens of body parts are continuously manufactured sequentially on welding jig lines. Once the panel is loaded onto the jig and clamped, welding typically begins within approximately four seconds, necessitating QI within that timeframe. The exploration of time intervals is described in Section 2.3.2 of the Methods part. The time required for the QI process is shown in Supplementary **Video 1**. MTS data values rapidly increase immediately after clamping, followed by an indication that the final quality judgment can be achieved within 2.79 s. Ultimately, the AI-assisted QI system successfully satisfied the time constraints required for implementation on the actual production line.

Supplementary material related to this article can be found online at doi:10.1016/j.jmsy.2025.07.001.

2.4. GUI environment

We developed a user-friendly GUI of the QI system to enhance usability. The GUI consists of two main components: the monitoring panels (Fig. 13**a, e**) and the control panels (Fig. 13**b-d**). Fig. 13**a** displays real-time sensor data for up to 10 sensors, with the option to add or remove sensors based on the user requirements. Fig. 13**b** presents a panel for collecting and labeling MTS data for AI model learning. The Auto Recording function can automatically detect the clamping status to initiate data acquisition, allowing for automatic storage of time-series data of a length suitable to the user's on-site conditions. The length of time-series data may vary depending on the required QI time in the industry and the trend of MTS data. Fig. 13**c** demonstrates the Model Generator feature. Clicking the 'Generate new model' button randomly extracts MTS data from pre-acquired normal and defective datasets to generate training and test datasets, initiating data preprocessing and model training. Upon the generation of the AI model, it is displayed as 'Model is ready' and ready for immediate use in QI. In Fig. 13**d**, the trend of real-time MTS data obtained right after clamping determines the defectiveness of the clamped parts and notifies the user accordingly. Finally, the clamping status can be monitored as shown in Fig. 13**c**. In conclusion, our GUI environment not only facilitates real-time monitoring for QI but also supports data collection and AI model generation for user convenience.

3. Experimental setup

3.1. Test jig setup and single-part preparation

Test welding jig and test parts were provided by a commercial automobile manufacturing company. The lab-made sensor modules were attached to four clamps in the test jig suitable for attachment. The wiring was routed along the jig surface and shielded to avoid contact with the welding machine. The shielded DAQ equipment was attached to a welding jig bed.

A total of ten test panels were prepared, with five serving as normal samples and the remaining five modified to represent realistic defects in various cases (Fig. 14). The defective samples were deformed to mimic the defective situation around the clamping spots for defect localization testing. To create a reference defective sample, a dimensional deviation of 500 μm was mimicked at the panel boundaries, an area with the most significant impact on product quality.

3.2. Welding jig setup on the production line and assembly-part preparation

This on-site verification was conducted at the door part production line of a commercial automobile manufacturer (Hyundai Motor Company), and a demonstration was performed on one of the welding jigs used in the actual vehicle door part production process. Clamps for sensor attachment were selectively placed at critical points affecting the quality of the part, with a total of eight sensors attached, four on each

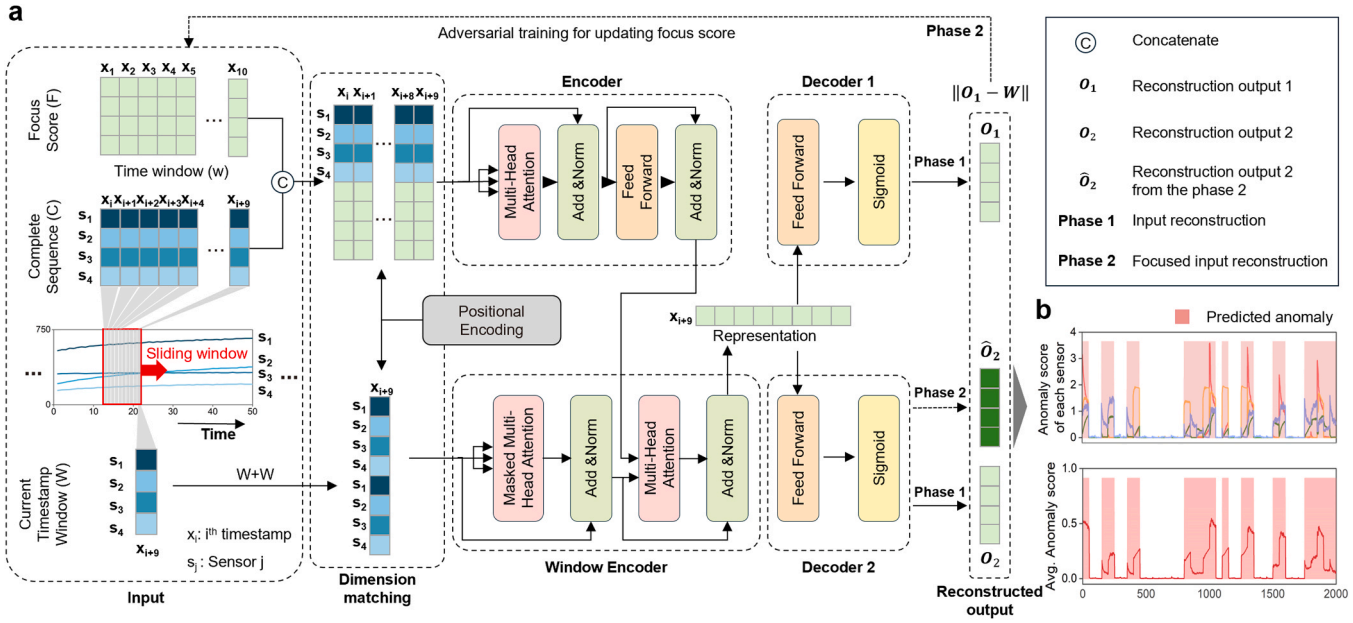

Fig. 11. Schematic diagram of the QuickDimML model.

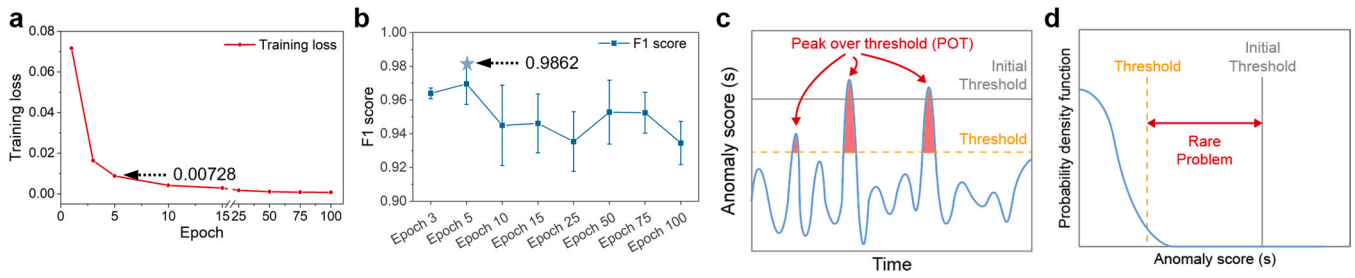

Fig. 12. Performance evaluation and threshold characterization results for QI.

Table 1
Performance comparison between QuickDimML and baseline methods (MAD-GAN, USAD, CAE-M) for 5 epochs. The best results are highlighted in bold.

	Training Time (s)	Precision	Recall	F1 Score
TranAD	**3.7288**	**0.9702**	**0.9999**	**0.9849**
MAD-GAN	57.7803	0.9146	0.9999	0.9554
USAD	43.3364	0.9294	0.9999	0.9634
CAE-M	36.6113	0.9410	0.9999	0.9696

side of the door part. Additionally, two dummy sensors were separately attached to adjust the height of the clamp contact surfaces (Fig. 15**b**).

To produce the door assembly, the inner panel and door member (DM) are loaded on the jig and then welded (Fig. 15**a**). Fig. 15**b** shows the door components loaded onto the jig before welding, and it shows the positions of sensors attached to the clamps. Fig. 15**c** and Fig. S2 show the eight combinations of assembly cases of the inner panels and DMs.

Provided test parts consist of inner panels, with two being normal and three being defective, and door members (DM), with one being normal and one being defective (Fig. 15**c** and Fig. S2). Defects in NG Part 1 and NG Part 3 were simulated by the experienced field worker and involved dents, bends, and twists. Additionally, NG Part 2 was sourced from defective parts discovered during the QI process of actual inner panel production using a checking fixture. NG Part 2 exhibits minute defects that are difficult to discern visually. The degree of defect increases in the order of NG Part 2, NG Part 1, and NG Part 3. In the case of the DM, it was bent at both ends, creating gaps and leading to imperfect contact when coupled with the inner panel on the welding jig.

4. Results and discussion

External factors such as equipment malfunctions and damaged part delivery to subsequent production lines can also contribute to these defects. Defects on the panel surface typically occur during the initial manufacturing stages [77], particularly due to imperfect springback in the pressing process [78,79]. While defects may occur sporadically at random locations, there is also the possibility of recurring defects at specific points. Therefore, quick identification of the defect location and understanding the variability in quality can significantly save costs, time, and manpower required for identifying the causes of defects when quality issues arise.

4.1. Demonstration of defect detection for a single part

As illustrated in Fig. 16, the real-time QI system enables the confirmation of individual sensor locations with high anomaly scores, allowing for the estimation of approximate defect locations. To assess the system's performance, defective panels were prepared with simulated defects around each of the four sensors, as depicted in Fig. 14. These five samples were sequentially loaded to the jig for a real-time defect detection demonstration, which can be observed in Supplementary **Video 2**. The MTS data measured during the demonstration are plotted in Fig. S3, with the normal data overlaid with each of the four defective data. The threshold for quality guarantee was set to 0.1, and if the average anomaly score exceeds threshold, the panel is classified as defective. The first graph in Fig. S3 shows the raw data of a normal panel and a panel with a defect near Sensor 1. Notable differences in sensor values and anomaly scores (Fig. 16**a**) are observed at the location of Sensor 1, where the defect is present. In contrast, Sensor 4, positioned furthest away from Sensor 1, shows no difference in trend between normal and defective conditions. The primary factors contributing to the increased anomaly scores include excessive clamping or poor contact between the door part and the clamp near defect sites. Additionally, due to the principle of the lever, sensors on the opposite side of the actual defect may also cause high anomaly scores. For instance, the difference between the anomaly scores of Sensors 1 and 3 could arise from these factors, as illustrated by Defective #1 in Fig. 16**a**. In the MTS and anomaly score graphs of Defective #2 (Fig. 16**a** and Fig. S3**)**, high anomaly scores are recorded at Sensors 2 and 3, which are close to the defective locations, while Sensors 1 and 4 show minimal differences from the normal range. Likewise, minimal variations of MTS data are observed at Sensor 4 for Defectives #1, # 2, and #3, whereas Defective #4 exhibits significant differences in the trend.

Supplementary material related to this article can be found online at doi:10.1016/j.jmsy.2025.07.001.

Accordingly, to evaluate whether the quality standards are satisfied, the average value of the overall anomaly scores from the sensors is used as the benchmark (Fig. 16**b**). Here, a threshold of 0.1 was set as the criterion for the presence of defects. Normal samples exhibited anomaly scores close to zero across all sensors and were classified as normal. In contrast, for the four types of defective samples, high anomaly scores were measured at sensors adjacent to defect locations, and the average anomaly scores exceeded the threshold, classifying them as defective.

4.2. Demonstration of defect detection for assembly part

Previously, the capability of detecting defects on a single panel and identifying their locations was confirmed using only four sensors on the test jig. Next, we conducted demonstrations with assembly door parts at the actual production line in an automotive manufacturing plant to verify the scalability and compatibility of our QI system.

In Supplementary **Video 3**, eight cases are tested in a random order a total of twelve times. The demonstration followed the sequence of cases ($1 \rightarrow 5 \rightarrow 6 \rightarrow 2 \rightarrow 8 \rightarrow 4 \rightarrow 2 \rightarrow 1 \rightarrow 7 \rightarrow 3 \rightarrow 4 \rightarrow 2$). The demonstration results show anomaly scores per sensor (Fig. 17**a**) and the average anomaly scores for each case (Fig. 17**b**). Anomaly scores for normal samples, corresponding to Case 1 and 2, both undergoing a total of five quality measurements, remain close to 0 with minimal variation (Fig. S4). Case 6, which combined a reference defective inner panel with a normal DM, shows the lowest anomaly score among the defective cases. A quality threshold of 0.150 was established for this demonstration, and the micro-dimensional defects in the reference sample exceeded this threshold by only 0.08. In Case 7, when defective DM is paired with the same inner panel as in Case 6, the anomaly score shows a further increase compared to the previous case (Fig. 17**b**). Defects around the welding joint points on DM cause abnormal pressure at the

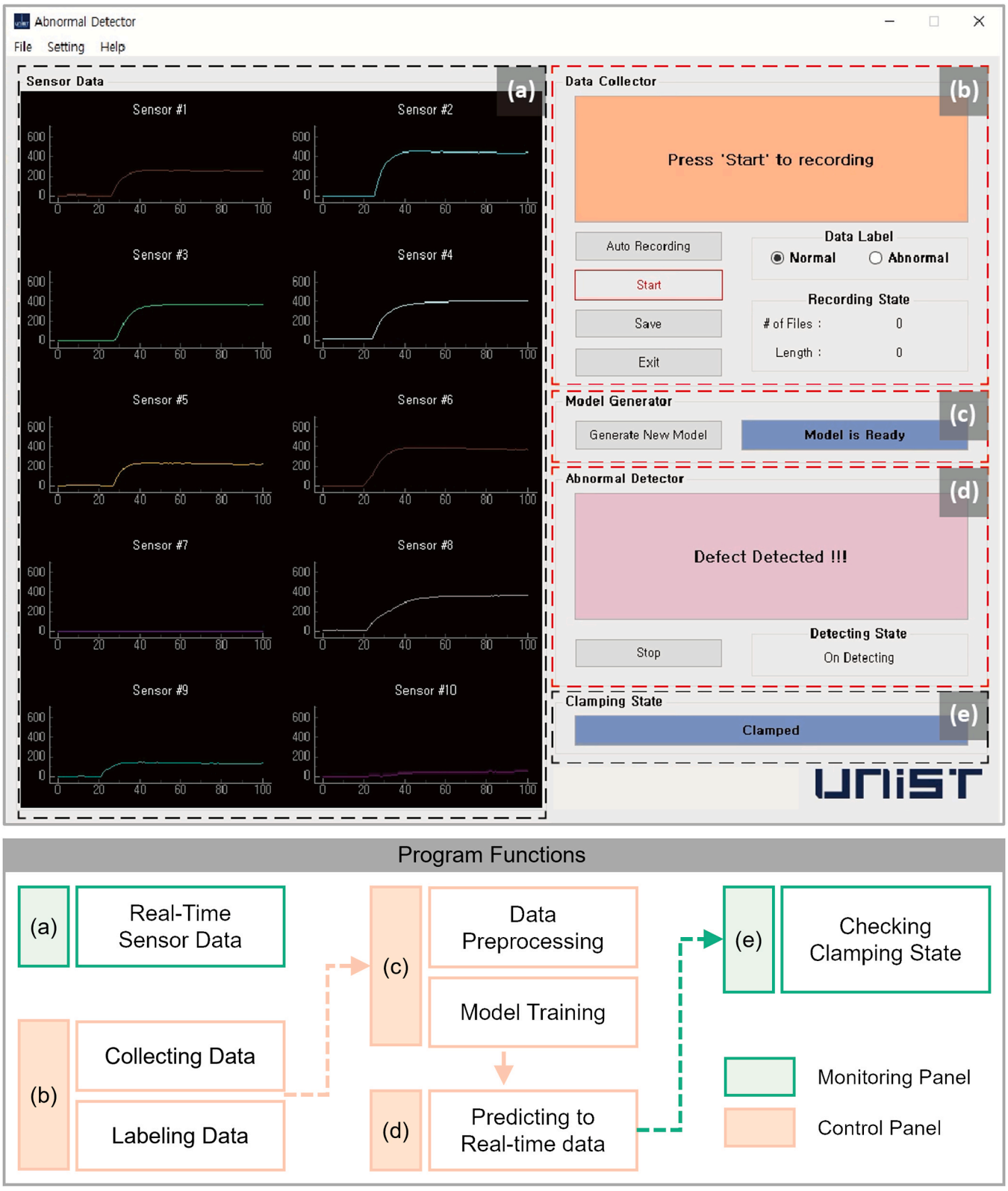

Fig. 13. GUI environment of anomaly detecting program. (a) Real-time sensor data plot, (b) Data collection and labeling panel, (c) Data preprocessing and model training function, (d) Anomaly detection for new real-time data, and (e), Checking clamping state.

contact surface with the inner panel, leading to changes in the trend of sensor values detected by nearby sensors.

Supplementary material related to this article can be found online at doi:10.1016/j.jmsy.2025.07.001.

To evaluate the quality of the DMs, we alternately combined normal and defective DMs with the same normal inner panel, assessing whether our system could effectively detect quality issues in the DMs. Testing Case 4 followed by Case 2, or Case 1 followed by Case 3, accurately and consistently revealed the influence of DM quality on the product. For both Case 3 and 4, the average anomaly scores remained consistently

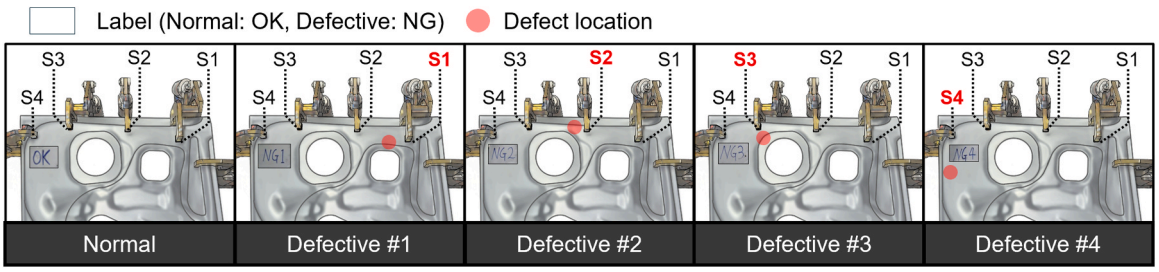

Fig. 14. The schematics of single door panels clamped on the test jig.

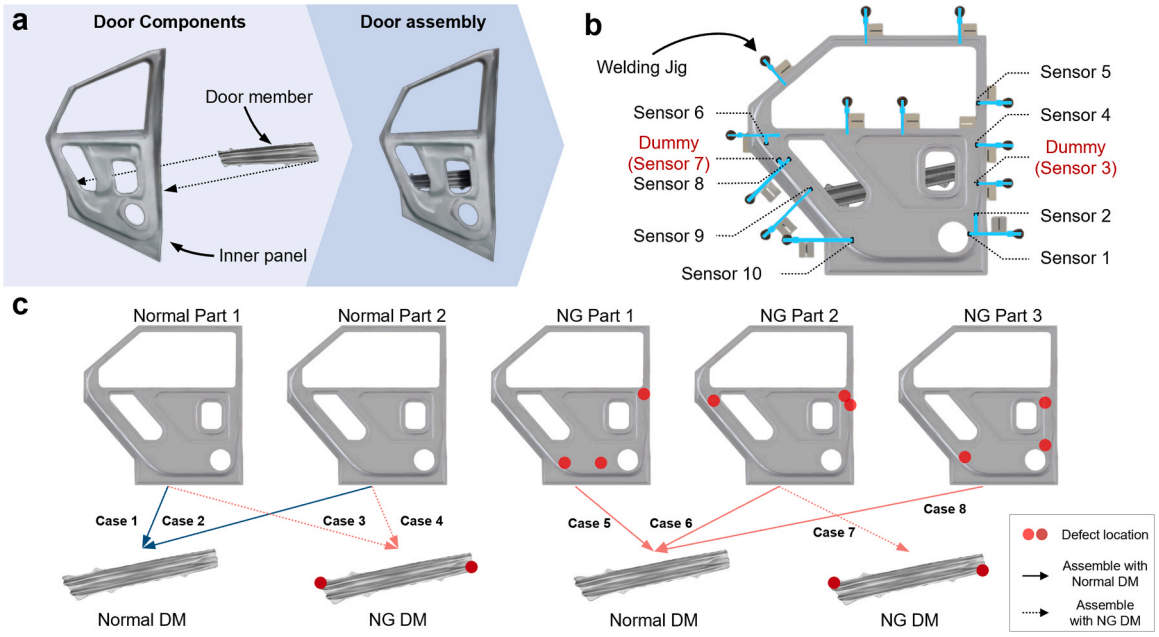

Fig. 15. The schematics of assembly parts composed of the inner panel and DM loaded on the welding jig setup on the production line.

close to 1.5 (Fig. 17**b**). The system was also evaluated to determine whether differences in anomaly scores could accurately reflect the severity of defects in the inner panel when using the same DM. The severity of the defect increases in the order of Case 6, Case 5, and Case 8, accompanied by corresponding increases in anomaly scores.

The model consistently demonstrated high performance during the field test, achieving an overall accuracy of 97.7 % (95 % confidence interval (CI): 96.12 %–98.61 %) across 30 trials per sample. The lowest recorded accuracy was 93.3 % for the sample with a 500 μm dimension error (95 % CI: 78.68 %–98.15 %), whereas the highest accuracy of 100 % was achieved where all 30 predictions were correct. However, due to production constraints, the same set of samples was used repeatedly in the field tests. While the model exhibited high predictive performance in both test dataset and field testing, the limited number of field samples may restrict the generalizability of the results.

4.3. *Visualization of defect locations*

Relying solely on anomaly score to identify defects can provide limited and non-intuitive information to field workers and may hinder prompt corrective actions. Visualizing defect locations on a virtual door panel as a heatmap allows workers to intuitively understand the extent and location of defects, facilitating quicker responses. In our approach, we mapped the potential defect regions onto the panel surface by plotting the average anomaly scores from each sensor at their respective positions. To visualize the anomaly score heatmap, we utilized the Matplotlib 3.7.5 in Python to overlay the heatmap onto the door panel image, ensuring precise alignment with the sensor positions. Since the anomaly scores are discrete, interpolation was employed using the SciPy 1.10.1 to generate a continuous heatmap representation. Figs. 18 and 19 present the visualized results based on defect detection data previously gathered from single parts (Fig. 16, Fig. 18) and the assembly parts (Figs. 17 and 19). The average anomaly scores for each sensor all time stamps are displayed in bar graphs (Fig. 18**b**). These values are applied to their corresponding sensor locations on a virtual door panel to create a heatmap (Fig. 18**c**). In the heat map, the highlighted defect locations closely match the actual defect positions, with areas of more severe defects emphasized in darker red.

In the assembly part, defects can arise not only in the inner panel but also from various issues related to the DM. Fig. 19**a, b** clearly show the characteristics observed when a defective DM is combined with a normal inner panel. The impact of the defective DM is also evident in Case 7 (Fig. 19**c, d**). Specifically, the anomaly scores of sensors 4, 5, 8, and 9, located near the DM joints, show a marked increase. A defective DM can cause bending in the inner panel fixed to the jig, leading to deformation in the central area of the panel. This consistent tendency is further supported by the anomaly scores per sensor in Fig. 19**b, c**, where sensors 4 and 8 exhibit increases in both cases. These results indicate that our system provides a highly consistent detection capability for similar types of defects. Moreover, the deformation in the center of the panel can be observed, caused by the abnormal pressure exerted by the DM on the inner panel. The visualization results from the defect location prediction simulation, based on anomaly scores from each sensor, effectively inform the approximate location and severity of defects to

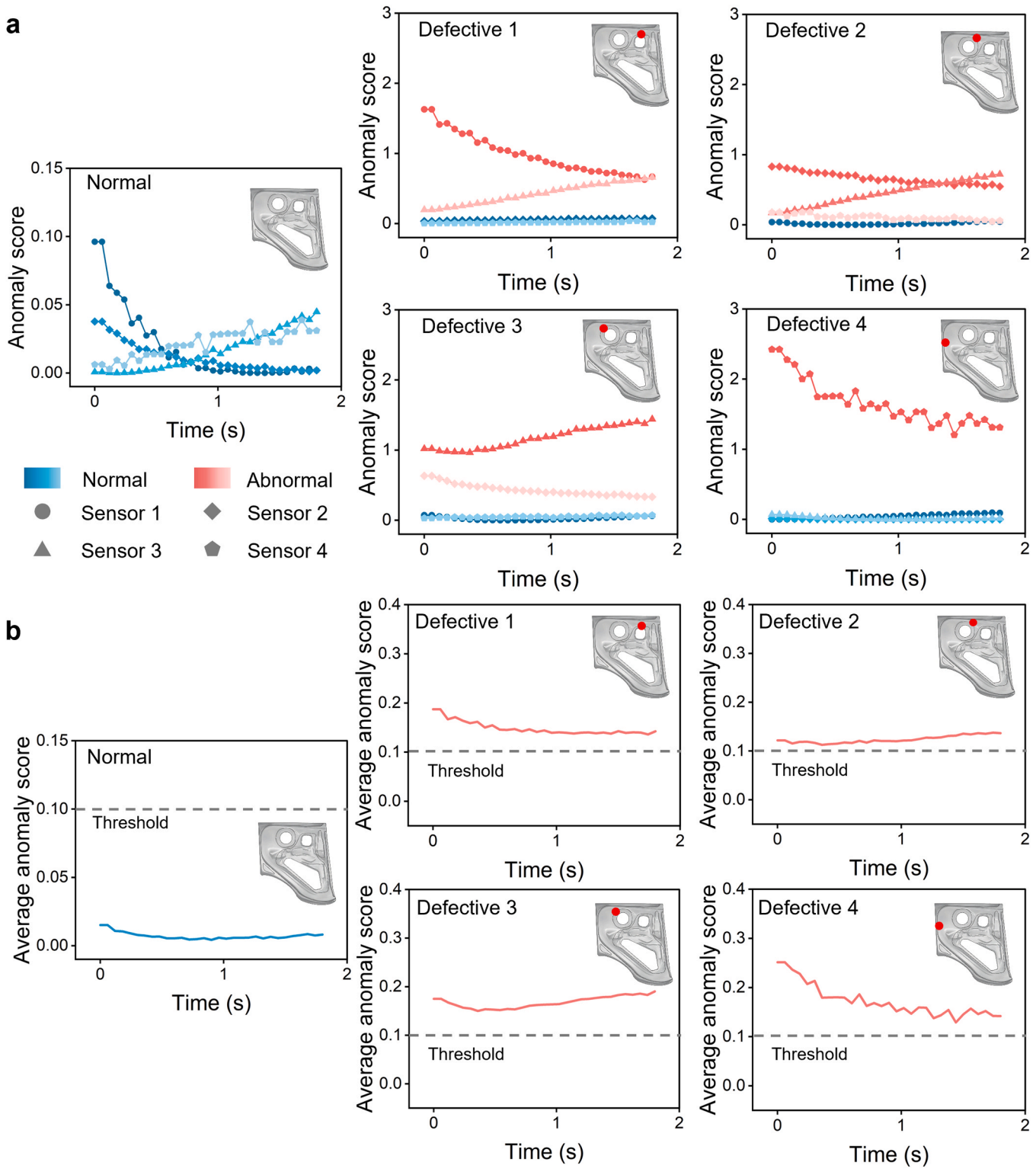

Fig. 16. Defect detection demonstration of the single parts. (a) Anomaly scores of MTS data measured from four sensors. (b) Average anomaly scores of MTS. Each data point represents the anomaly score at the corresponding time point.

workers. Ultimately, the demonstration across 12 tests of 8 cases, as shown in Supplementary **Video 3,** successfully differentiated between defective and normal samples. The anomaly scores are obtained from the clamp positions, where multiple parts come into contact and welding is primarily performed, making these regions prone to most defects. However, due to the lack of direct measurements, defects away from the clamps are represented by interpolated values, potentially enlarging the estimated defect locations.

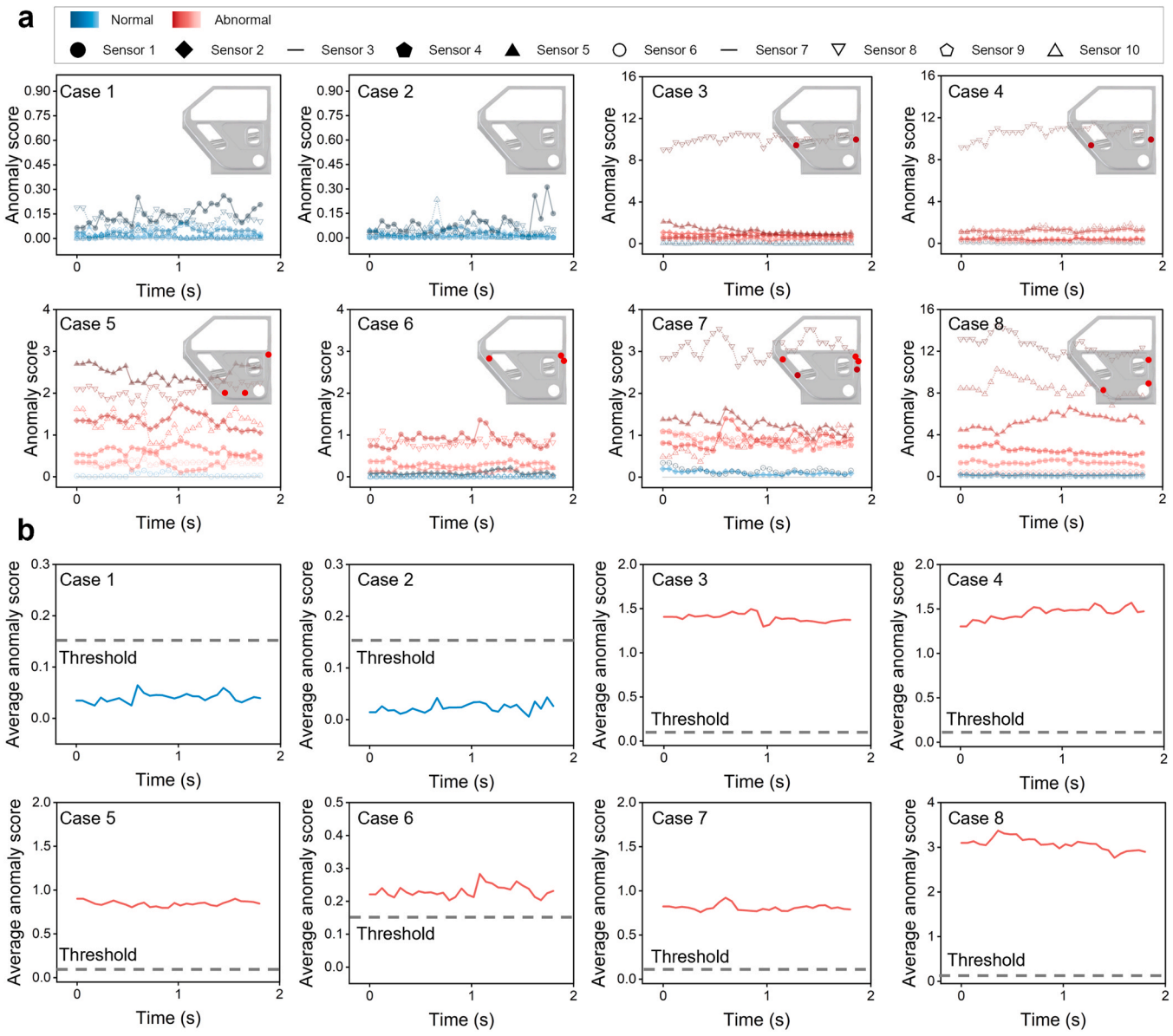

Fig. 17. Defect detection demonstration of the assembly-parts. (a) Anomaly scores of MTS data measured from eight sensors. (b) Average anomaly scores of MTS data measured from each sensor.

4.4. Discussion

Our work applied an unsupervised ML model for total QI, achieving an F1 score of 0.9862, effectively eliminating uninspected defective products and human factor errors, issues commonly associated with traditional QI, which relies on random sampling and manual inspections. Humans conduct QI on randomly sampled products, which can result in undetected defects due to uninspected products and human factor errors. AI-based QI allows for total inspection of all products, detecting all defects except for a few wrong predictions. We anticipate that implementing total QI across all 300,000 sub-assemblies corresponding to the total production will significantly enhance quality reliability (Fig. 20**a, c**). Random sampling with manual QI results in irregular accuracy for a small number of products [19,20] , whereas our method achieves an F1 score of 0.9862 for the total inspection. This advancement is projected to reduce QI costs by 20 %. Moreover, AI-based QI provides results in under 3 s, significantly reducing time compared to manual inspections that require multiple procedures and take several minutes [17,18] to just 2.79 s per product (Fig. 20**b**), making total QI feasible. This improvement is projected to save approximately 3 million dollars annually by reducing the costs associated with poor-quality products and quality corrections (Fig. 20**c**).

5. Conclusion

We report a real-time, automated QI system to detect micrometer-scale dimensional deviations in parts loaded onto welding jigs during automotive sub-assembly production. The sensing system utilizes 3D-printed sensor caps embedded with strain gauges made from high-elasticity TPU, that are highly responsive to shape changes under clamping pressure. These sensor caps, attached to welding jig clamps, compress to conform to the door panel shape when the jig clamps the parts, enabling them to detect strain differences caused by dimensional errors as small as 500 μm.

Our approach employs a deep-transformer network algorithm to detect anomalies in MTS data collected from multiple clamps, providing a quality status notification to the operator within 2.79 s, thus maintaining production speed. Using only MTS data from normal panels

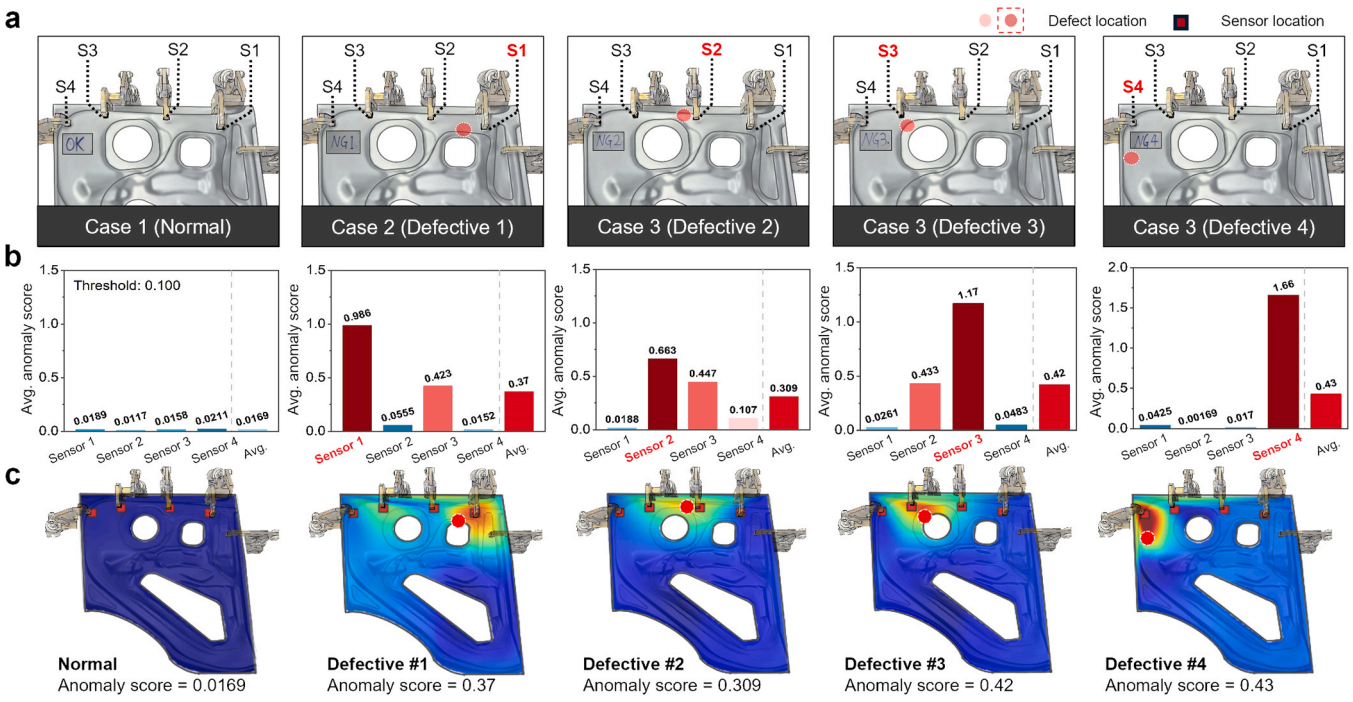

Fig. 18. Comparison of the predicted and actual defect location for single-part cases.

collected during the first three seconds of clamping, we achieved an F1 score of 0.9862 with five epochs of training, outperforming other baseline methods in accuracy and computational speed. We simulated various defects occurring at random locations across two welding jigs and their corresponding parts, successfully demonstrating the system's capability to detect these defects accurately. The system also evaluates defect locations and severity based on anomaly scores from the MTS data of sensors attached to clamps at multiple panel positions.

Furthermore, the system provides defect localization via heatmap visualization of anomaly scores from each sensor, assisting workers in the rapid identification and resolution of issues. This QI system is versatile and adaptable to various vehicle models and sub-assembly lines, indicating potential for enhanced productivity, simplified processes, and cost savings compared to manual inspection or non-contact coordinate measuring machines.

Nevertheless, although the feasibility of the proposed system has been demonstrated, challenges remain for large-scale commercialization due to the limitations of the current 3D printing-based sensor fabrication process, and the restricted clamp placement on the jig affecting defect localization. Therefore, to enable the large-scale and long-term implementation of the proposed QI system in industrial manufacturing environments, further optimization of core components is necessary. Future research will focus on improving the mechanical durability and fabrication consistency of the sensor caps to ensure stable performance under high-cycle operation. In parallel, optimized sensor placement strategies, such as full utilization of existing clamps or strategic addition of new sensing points, will be investigated to enhance the detection accuracy of localized defects across the panel and reduce false positives. Addressing these challenges is expected to improve both the reliability and scalability of real-time quality inspection systems in actual production settings.

The extensive quality data generated during production will also serve as a foundation for future comprehensive factory-wide quality diagnostics, management, and improvement through digital systems.

CRediT authorship contribution statement

Seobin Park: Investigation, Writing – original draft, Software, Data curation, Visualization, Methodology, Writing – review & editing, Validation, Conceptualization. **Wooseok Ji:** Formal analysis, Methodology, Software. **Im Doo Jung:** Conceptualization, Supervision, Funding acquisition, Visualization, Project administration, Writing – review & editing, Writing – original draft, Validation, Methodology, Investigation. **Kyeong Min Kim:** Conceptualization, Writing – original draft, Validation, Supervision, Resources, Project administration, Methodology, Investigation. **Junyoung Seo:** Validation, Software, Data curation, Methodology. **Jongwon Chung:** Conceptualization, Supervision, Resources, Project administration, Funding acquisition. **Jeong Ho Choi:** Validation, Project administration, Supervision, Resources, Methodology, Conceptualization. **Taekyeong Kim:** Validation, Conceptualization, Software, Writing – review & editing, Writing – original draft, Visualization, Investigation, Methodology, Data curation.

Code availability

The source code for QuickDimML is classified as a secure resource of the company. Therefore, access to the code is restricted and can only be provided upon reasonable request to the corresponding authors.

Declaration of Competing Interest

The authors declare that they have no known competing financial interests or personal relationships that could have appeared to influence the work reported in this paper.

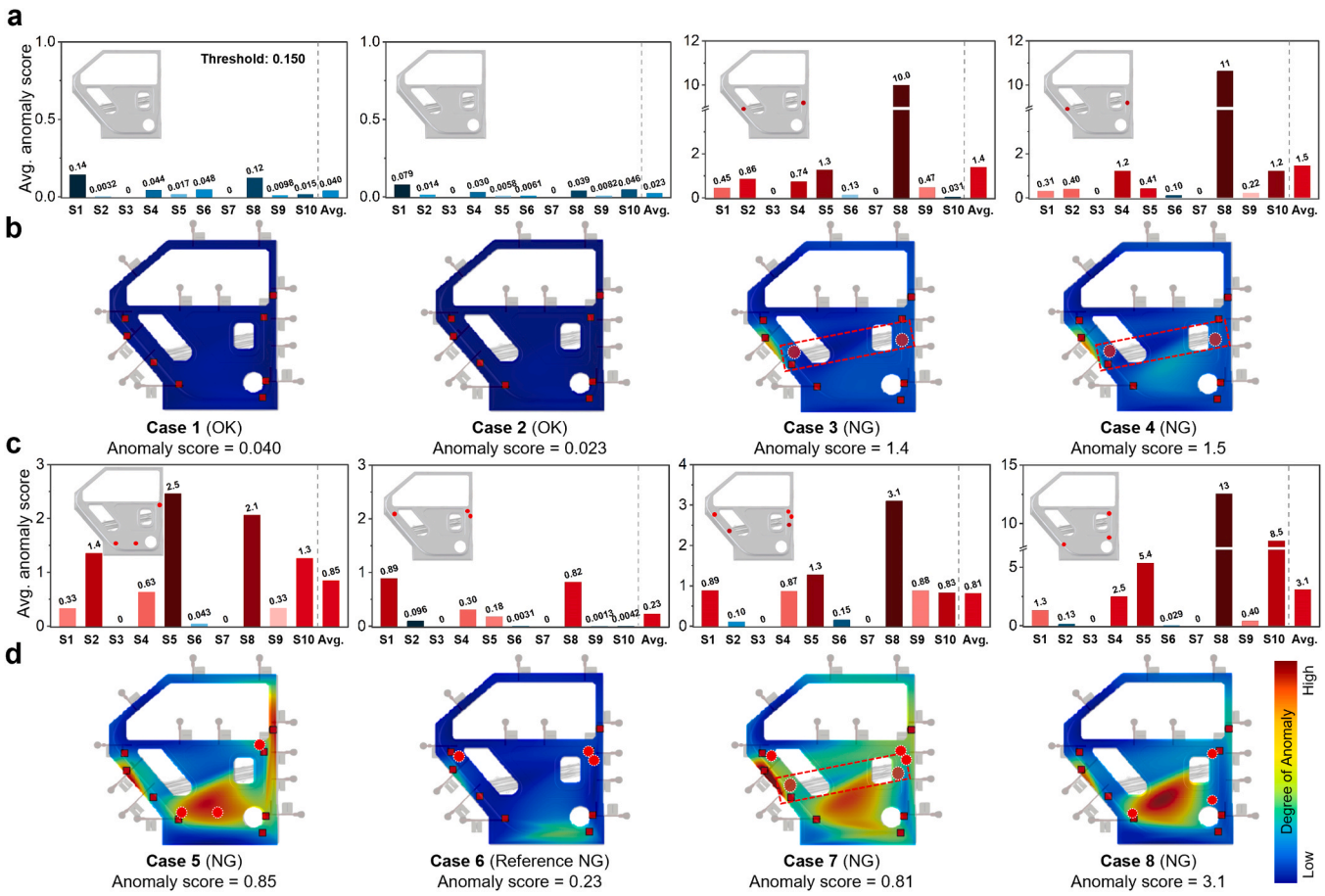

Fig. 19. Comparison of the predicted and actual defect location for assembly-part cases. (Bright red circle: defects on the inner panel, dark red circle with dashed box: defects on the DM).

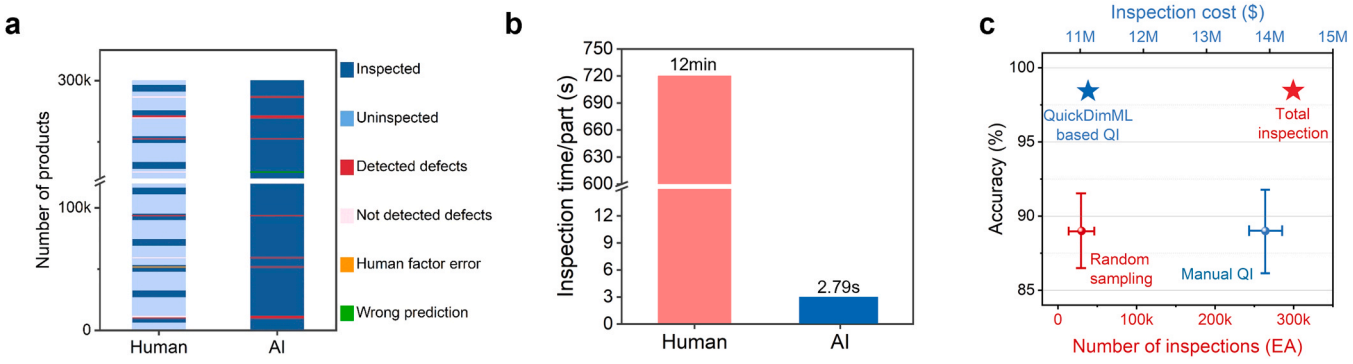

Fig. 20. The expected benefits of introducing a novel QI System.

Acknowledgements

This research was supported by Hyundai Motor Company and Hyundai NGV. This work was supported by the Technology development Program (Grant No. S3248116) funded by the Ministry of SMEs and Startups (MSS, Korea), the National Research Foundation of Korea (NRF) grant funded by the Korea government (MSIT) (Nos. RS-2024–00416891, RS-2023–00211636), and the Institute of Information & Communications Technology Planning & Evaluation (IITP) grant funded by the Korea government (MSIT) (No. RS-2020-II201336, Artificial Intelligence Graduate School Program (UNIST)).

Appendix A. Supporting information

Supplementary data associated with this article can be found in the online version at doi:10.1016/j.jmsy.2025.07.001.

References

[1] Li J, Li X, Yardimci NT, Hu J, Li Y, Chen J, Hung Y-C, Jarrahi M, Ozcan A. Rapid sensing of hidden objects and defects using a single-pixel diffractive terahertz sensor. Nat Commun 2023;14(1):6791.

[2] Azamfirei V, Psarommatis F, Lagrosen Y. Application of automation for in-line quality inspection, a zero-defect manufacturing approach. J Manuf Syst 2023;67:1–22.

[3] Psarommatis F, May G, Dreyfus P-A, Kiritsis D. Zero defect manufacturing: state-of-the-art review, shortcomings and future directions in research. Int J Prod Res 2020;58(1):1–17.
[4] Ng WL, Goh GL, Goh GD, Ten JSJ, Yeong WY. Progress and opportunities for machine learning in materials and processes of additive manufacturing. Adv Mater 2024:2310006.
[5] Mu X, Wang Y, Yuan B, Sun W, Liu C, Sun Q. A New assembly precision prediction method of aeroengine high-pressure rotor system considering manufacturing error and deformation of parts. J Manuf Syst 2021;61:112–24.
[6] Wang P, Zhang Q, Qu H, Xu X, Yang S. Time series prediction for production quality in a machining system using spatial-temporal multi-task graph learning. J Manuf Syst 2024;74:157–79.
[7] Mumbelli JD, Guarneri GA, Lopes YK, Casanova D, Teixeira M. An application of generative adversarial networks to improve automatic inspection in automotive manufacturing. Appl Soft Comput 2023;136:110105.
[8] Park J, Min KM, Kim H, Hong SH, Lee MG. Integrated computational materials engineering for advanced automotive technology: with focus on life cycle of automotive body structure. Adv Mater Technol 2023;8(20):2201057.
[9] Shin HG, Timilsina S, Sohn KS, Kim JS. Digital image correlation compatible mechanoluminescent skin for structural health monitoring. Adv Sci 2022;9(11):2105889.
[10] Moon J, Bae G, Jeong B-Y, Shin C, Kwon M-J, Kim D-I, Choi D-J, Lee BH, Lee C-H, Hong H-U. Ultrastrong and ductile steel welds achieved by fine interlocking microstructures with film-like retained austenite. Nat Commun 2024;15(1):1301.
[11] Wang Q, Zhao Y, Zhao T, Yan D, Wang G, Wu A. Influence of restraint conditions on residual stress and distortion of 2219-T8 aluminum alloy TIG welded joints based on contour method. J Manuf Process 2021;68:796–806.
[12] Ma Y, Chen G, Lv M, Yi W, Liu X, Chen H, Zhu B. Efficient and effective dimension control in automotive applications. IEEE Trans Ind Inform 2020;17(3):1583–91.
[13] Lian J, Lai X, Lin Z, Yao F. Application of data mining and process knowledge discovery in sheet metal assembly dimensional variation diagnosis. J Mater Process Technol 2002;129(1-3):315–20.
[14] Lu Y, Xu X, Wang L. Smart manufacturing process and system automation–a critical review of the standards and envisioned scenarios. J Manuf Syst 2020;56:312–25.
[15] Siva R, Purusothaman M. Reducing the frequency of inspection in an automobile industry by quality tool. Int J Appl Eng Res 2015;10(61).
[16] Alves JB, Marques B, Dias P, Santos BS. Using augmented reality for industrial quality assurance: a shop floor user study. Int J Adv Manuf Technol 2021;115(1):105–16.
[17] Zhou Q, Chen R, Huang B, Liu C, Yu J, Yu X. An automatic surface defect inspection system for automobiles using machine vision methods. Sensors 2019;19(3):644.
[18] Molina J, Solanes JE, Arnal L, Tornero J. On the detection of defects on specular car body surfaces. Robot ComputIntegr Manuf 2017;48:263–78.
[19] Tjolleng A, Chang J, Park J, Lee W, Cha M, Park J, Jung K. Development of a human-friendly visual inspection method for painted vehicle bodies. Appl Ergon 2023;106:103911.
[20] Martínez SS, Vázquez CO, García JG, Ortega JG. Quality inspection of machined metal parts using an image fusion technique. Measurement 2017;111:374–83.
[21] Ashwini K, Rudraswamy S. Automated inspection system for automobile bearing seals. Mater Today Proc 2021;46:4709–15.
[22] Pfeiffer S. Robots, Industry 4.0 and humans, or why assembly work is more than routine work. Societies 2016;6(2):16.
[23] Kim G, Choi JG, Ku M, Lim S. Developing a semi-supervised learning and ordinal classification framework for quality level prediction in manufacturing. Comput Ind Eng 2023;181:109286.
[24] Wang J, Ma Y, Zhang L, Gao RX, Wu D. Deep learning for smart manufacturing: methods and applications. J Manuf Syst 2018;48:144–56.
[25] Chen G, Sheng B, Luo R, Jia P. A parallel strategy for predicting the quality of welded joints in automotive bodies based on machine learning. J Manuf Syst 2022;62:636–49.
[26] Kiraci E, Palit A, Donnelly M, Attridge A, Williams MA. Comparison of in-line and off-line measurement systems using a calibrated industry representative artefact for automotive dimensional inspection. Measurement 2020;163:108027.
[27] Yang R, Singh SK, Tavakkoli M, Amiri N, Yang Y, Karami MA, Rai R. CNN-LSTM deep learning architecture for computer vision-based modal frequency detection. Mech Syst Signal Process 2020;144:106885.
[28] Chen J, Zhang Z, Wu F. A data-driven method for enhancing the image-based automatic inspection of IC wire bonding defects. Int J Prod Res 2021;59(16):4779–93.
[29] Kholkhujaev J, Maculotti G, Genta G, Galetto M, Inoyatkhodjaev J. Non-contact articulated robot-integrated gap and flushness measurement system for automobile assembly. IEEE Access 2022;10:86528–41.
[30] Hua S, Li B, Shu L, Jiang P, Cheng S. Defect detection method using laser vision with model-based segmentation for laser brazing welds on car body surface. Measurement 2021;178:109370.
[31] Guo J, Wang Q, Park J-H. Geometric quality inspection of prefabricated MEP modules with 3D laser scanning. Autom Constr 2020;111:103053.
[32] Oh S, You J-H, Eskandarian A, Kim Y-K. Accurate alignment inspection system for low-resolution automotive LiDAR. IEEE Sens J 2021;21(10):11961–8.
[33] Seo E, Sung H, Jeon H, Kim H, Kim T, Park S, Lee MS, Moon SK, Kim JG, Chung H. Laser powder bed fusion for AI assisted digital metal components. Virtual Phys Prototyp 2022;17(4):806–20.
[34] Lee MS, Lee J, Sung H, Choe J, Son HJ, Yun J, Kim K-b, Kim M, Lee SW, Yang S. Embedding sensors using selective laser melting for self-cognitive metal parts. Addit Manuf 2020;33:101151.
[35] Cai B, Hao K, Wang Z, Yang C, Kong X, Liu Z, Ji R, Liu Y. Data-driven early fault diagnostic methodology of permanent magnet synchronous motor. Expert Syst Appl 2021;177:115000.
[36] Quatrini E, Costantino F, Di Gravio G, Patriarca R. Machine learning for anomaly detection and process phase classification to improve safety and maintenance activities. J Manuf Syst 2020;56:117–32.
[37] Wang J, Liang Y, Zheng Y, Gao RX, Zhang F. An integrated fault diagnosis and prognosis approach for predictive maintenance of wind turbine bearing with limited samples. Renew Energy 2020;145:642–50.
[38] Park J, Hamadache M, Ha JM, Kim Y, Na K, Youn BD. A positive energy residual (PER) based planetary gear fault detection method under variable speed conditions. Mech Syst Signal Process 2019;117:347–60.
[39] Rohan A, Raouf I, Kim HS. Rotate vector (RV) reducer fault detection and diagnosis system: towards component level prognostics and health management (PHM). Sensors 2020;20(23):6845.
[40] Raouf I, Lee H, Kim HS. Mechanical fault detection based on machine learning for robotic RV reducer using electrical current signature analysis: a data-driven approach. J Comput Des Eng 2022;9(2):417–33.
[41] R. Chalapathy, S. Chawla, Deep learning for anomaly detection: A survey, arXiv preprint arXiv:1901.03407 (2019).
[42] Bao X, Zheng Y, Chen L, Wu D, Chen X, Liu Y. Abnormal pattern recognition for online inspection in manufacturing process based on multi-scale time series classification. J Manuf Syst 2024;76:457–77.
[43] Martínez-Arellano G, Terrazas G, Ratchev S. Tool wear classification using time series imaging and deep learning. Int J Adv Manuf Technol 2019;104:3647–62.
[44] Theissler A. Detecting known and unknown faults in automotive systems using ensemble-based anomaly detection. KnowlBased Syst 2017;123:163–73.
[45] Canizo M, Triguero I, Conde A, Onieva E. Multi-head CNN–RNN for multi-time series anomaly detection: An industrial case study. Neurocomputing 2019;363:246–60.
[46] Xie X, Wang B, Wan T, Tang W. Multivariate abnormal detection for industrial control systems using 1D CNN and GRU. Ieee Access 2020;8:88348–59.
[47] Maldonado-Correa J, Torres-Cabrera J, Martín-Martínez S, Artigao E, Gómez-Lázaro E. Wind turbine fault detection based on the transformer model using SCADA data. Eng Fail Anal 2024;162:108354.
[48] Santoro A, Battiston F, Petri G, Amico E. Higher-order organization of multivariate time series. Nat Phys 19(2 2023:221–9.
[49] Kim G, Choi JG, Lim S. Using transformer and a reweighting technique to develop a remaining useful life estimation method for turbofan engines. Eng Appl Artif Intell 2024;133:108475.
[50] Orabi M, Tran KP, Egger P, Thomassey S. Anomaly detection in smart manufacturing: an adaptive adversarial transformer-based model. J Manuf Syst 2024;77:591–611.
[51] Tian Z, Zhuo M, Liu L, Chen J, Zhou S. Anomaly detection using spatial and temporal information in multivariate time series. Sci Rep 2023;13(1):4400.
[52] Massari L, Fransvea G, D'Abbraccio J, Filosa M, Terruso G, Aliperta A, D'Alesio G, Zaltieri M, Schena E, Palermo E. Functional mimicry of Ruffini receptors with fibre Bragg gratings and deep neural networks enables a bio-inspired large-area tactile-sensitive skin. Nat Mach Intell 2022;4(5):425–35.
[53] S. Tuli, G. Casale, N.R. Jennings, Tranad: Deep transformer networks for anomaly detection in multivariate time series data, arXiv preprint arXiv:2201.07284 (2022).
[54] Kiangala KS, Wang Z. An effective predictive maintenance framework for conveyor motors using dual time-series imaging and convolutional neural network in an industry 4.0 environment. Ieee Access 2020;8:121033–49.
[55] Yang C-L, Chen Z-X, Yang C-Y. Sensor classification using convolutional neural network by encoding multivariate time series as two-dimensional colored images. Sensors 2019;20(1):168.
[56] Kim H, Lee J, Kim T, Park SJ, Kim H. Advanced thermal fluid leakage detection system with machine learning algorithm for pipe-in-pipe structure. Case Stud Therm Eng 2023;42:102747.
[57] Audibert J, Michiardi P, Guyard F, Marti S, Zuluaga MA. Usad: Unsupervised anomaly detection on multivariate time series. Proc 26th ACM SIGKDD Int Conf Knowl Discov data Min 2020:3395–404.
[58] Li D, Chen D, Jin B, Shi L, Goh J, Ng S-K. MAD-GAN: Multivariate anomaly detection for time series data with generative adversarial networks. International conference on artificial neural networks. Springer; 2019. p. 703–16.
[59] Zheng M, Man J, Wang D, Chen Y, Li Q, Liu Y. Semi-supervised multivariate time series anomaly detection for wind turbines using generator SCADA data. Reliab Eng Syst Saf 2023;235:109235.
[60] Vaswani A, Shazeer N, Parmar N, Uszkoreit J, Jones L, Gomez AN, Kaiser Ł, Polosukhin I. Attention is all you need. Adv Neural Inf Process Syst 2017;30.
[61] Pillai SD, Goldfarb B, Kirsch DA. The origins of firm strategy: learning by economic experimentation and strategic pivots in the early automobile industry. Strateg Manag J 2020;41(3):369–99.
[62] Greco A, Russo MB, Gerbino S. Simultaneous impact of build orientation on mechanical properties, geometrical measurements and surface roughness in material extrusion manufacturing. Rapid Prototyp J 2024;31(11):1–27.
[63] García Plaza E, López PJN, Torija MÁC, Muñoz JMC. Analysis of PLA geometric properties processed by FFF additive manufacturing: effects of process parameters and plate-extruder precision motion. Polymers 2019;11(10):1581.
[64] Shakeri Z, Benfriha K, Zirak N, Shirinbayan M. Mechanical strength and shape accuracy optimization of polyamide FFF parts using grey relational analysis. Sci Rep 2022;12(1):13142.
[65] Xu H, Li H, Xiang G, Zhang X. An improved adaptive surrogate model and application in thermal management system design. Mater Des 2021;208:109883.

[66] Fuhg JN, Fau A, Nackenhorst U. State-of-the-art and comparative review of adaptive sampling methods for kriging. Arch Comput Methods Eng 2021;28:2689–747.
[67] Russo MB, Franciosa P, Greco A, Gerbino S. Reduced-order modelling for real-time physics-based variation simulation enhanced with adaptive sampling and optimized interpolation. Int J Adv Manuf Technol 2024;132(7):3709–34.
[68] Akşehir ZD, Kilic E. How to handle data imbalance and feature selection problems in CNN-based stock price forecasting. IEEE Access 2022;10:31297–305.
[69] Kim T, Moon NH, Goh TS, Jung ID. Detection of incomplete atypical femoral fracture on anteroposterior radiographs via explainable artificial intelligence. Sci Rep 2023;13(1):10415.
[70] Jiang J-R, Chen Y-T. Industrial control system anomaly detection and classification based on network traffic. IEEE Access 2022;10:41874–88.
[71] Kang H, Kang P. Transformer-based multivariate time series anomaly detection using inter-variable attention mechanism. KnowlBased Syst 2024:111507.
[72] Kim S, Choi K, Choi H-S, Lee B, Yoon S. Towards a rigorous evaluation of time-series anomaly detection. Proc AAAI Conf Artif Intell 2022:7194–201.
[73] D. Kinga, J.B. Adam, A method for stochastic optimization, International conference on learning representations (ICLR), San Diego, California;, 2015.
[74] Zhang Y, Chen Y, Wang J, Pan Z. Unsupervised deep anomaly detection for multi-sensor time-series signals. IEEE Trans Knowl Data Eng 35(2 2021:2118–32.
[75] Siffer A, Fouque P-A, Termier A, Largouet C. Anomaly detection in streams with extreme value theory. Proc 23rd ACM SIGKDD Int Conf Knowl Discov data Min 2017:1067–75.
[76] Su Y, Zhao Y, Niu C, Liu R, Sun W, Pei D. Robust anomaly detection for multivariate time series through stochastic recurrent neural network. Proc 25th ACM SIGKDD Int Conf Knowl Discov data Min 2019:2828–37.
[77] Zhou C, Lu Z, Lv Z, Meng M, Tan Y, Xia K, Liu K, Zuo H. Metal surface defect detection based on improved YOLOv5. Sci Rep 2023;13(1):20803.
[78] Firat M, Kaftanoglu B, Eser O. Sheet metal forming analyses with an emphasis on the springback deformation. J Mater Process Technol 2008;196(1-3):135–48.
[79] Miao Y, Jeon JY, Park G. An image processing-based crack detection technique for pressed panel products. J Manuf Syst 2020;57:287–97.